Airborne observations of the surface cloud radiative effect during different seasons over sea ice and open ocean in the Fram Strait

Sebastian Becker[1], André Ehrlich[1], Michael Schäfer[1], and Manfred Wendisch[1]

[1]Leipzig Institute for Meteorology (LIM), Leipzig University, Leipzig, Germany

Correspondence: Sebastian Becker (sebastian.becker@uni-leipzig.de)

Abstract. This study analyzes the cloud radiative effect (CRE) obtained from near-surface observations of three airborne campaigns in the Arctic north-west of Svalbard: AFLUX (March/April 2019), ACLOUD (May/June 2017), and MOSAiC-ACA (August/September 2020). The surface CRE quantifies the potential of clouds to modify the radiative energy budget at the surface and is calculated by combining broadband radiation measurements during low-level flight sections in mostly cloudy conditions with radiative transfer simulations of cloud-free conditions. The significance of surface albedo changes due to the presence of clouds is demonstrated and this effect is considered in the cloud-free simulations. The observations are discussed with respect to differences of the CRE between sea ice and open ocean surfaces, and between the seasonally different campaigns. The results indicate that the CRE depends on both cloud, illumination, surface, and thermodynamic properties. The solar and thermal-infrared (TIR) components of the CRE, CRE_{sol} and CRE_{TIR}, are analyzed separately as well as combined for the study of the total CRE (CRE_{tot}). The inter-campaign differences of CRE_{sol} are dominated by the seasonal cycle of the solar zenith angle, with the strongest cooling effect in summer. The lower surface albedo causes a stronger solar cooling effect over open ocean than over sea ice, which amounts to $-259\,\mathrm{W\,m^{-2}}$ ($-108\,\mathrm{W\,m^{-2}}$) and $-65\,\mathrm{W\,m^{-2}}$ ($-17\,\mathrm{W\,m^{-2}}$), respectively, during summer (spring). Independent of campaign and surface type, CRE_{TIR} is only weakly variable and shows values around $75\,\mathrm{W\,m^{-2}}$. In total, clouds show a negative CRE_{tot} over open ocean during all campaigns. In contrast, over sea ice, the positive CRE_{tot} suggests a warming effect of clouds at the surface, which neutralizes during mid-summer. Given the seasonal cycle of the sea ice distribution, these results imply that clouds in the Fram Strait region cool the surface during the sea ice minimum in late summer, while they warm the surface during the sea ice maximum in spring.

1 Introduction

The enhanced warming and the rapid loss of sea ice are the most obvious signs of accelerated climate changes currently ongoing in the Arctic. Because these changes appear much faster compared to the rest of the globe, the term Arctic amplification was introduced (Serreze and Barry, 2011; Wendisch et al., 2017, 2022a). A multitude of atmospheric processes and feedback mechanisms contributes to this amplified transformation of the Arctic climate system. Clouds play a substantial, yet not fully understood, role in Arctic amplification by their involvement in several feedbacks. For example, the downward radiative energy

fluxes in the thermal-infrared (TIR) range[1] (~ 4–$100\,\mu\text{m}$) are increased by clouds, which leads to a warmer surface and delayed refreezing, thinner sea ice, and faster melting (positive cloud–sea ice feedback, Morrison et al., 2019). At the same time, the increased fraction of liquid water in the clouds increases the cloud optical thickness and the reflection of solar[1] radiation (~ 0.3–$4\,\mu\text{m}$) by the cloud (negative cloud optical thickness feedback, e. g., Zelinka et al., 2012; Ceppi et al., 2015). Furthermore, the indirect influence of clouds on other feedbacks is demonstrated by the reduction of the sea ice–albedo feedback in summer through increased cloud fraction or optical thickness (Kay et al., 2012; Choi et al., 2020). This multitude of partly opposing effects complicates the evaluation of the combined impact of clouds within the Arctic climate system and makes the sign (warming or cooling) of the total cloud feedback uncertain (Forster et al., 2021).

In consequence, a realistic representation of the impact of clouds within the Arctic climate system in numerical weather and climate models appears crucial. In particular, the radiative energy budget (REB) of the surface and the atmosphere is largely determined by the presence and properties of clouds (Wendisch et al., 2022b). The surface REB is investigated separately for the solar and TIR ranges and quantified by the broadband solar and TIR net irradiances, $F_{\text{net,sol}}$ and $F_{\text{net,TIR}}$. They are defined as the difference of the respective broadband downward ($F_{\text{sol}}^{\downarrow}$ and $F_{\text{TIR}}^{\downarrow}$) and upward ($F_{\text{sol}}^{\uparrow}$ and $F_{\text{TIR}}^{\uparrow}$) irradiances:

$$F_{\text{net,sol}} = F_{\text{sol}}^{\downarrow} - F_{\text{sol}}^{\uparrow}, \tag{1}$$

$$F_{\text{net,TIR}} = F_{\text{TIR}}^{\downarrow} - F_{\text{TIR}}^{\uparrow}. \tag{2}$$

The cloud impact on the REB is quantified by the solar and TIR cloud radiative effect (CRE), CRE_{sol} and CRE_{TIR}, respectively, which is also reffered to as cloud raditive forcing (Ramanathan et al., 1989). It is derived from the difference of the net irradiances in cloudy ($F_{\text{net,sol,cld}}$ and $F_{\text{net,TIR,cld}}$) and cloud-free ($F_{\text{net,sol,cf}}$ and $F_{\text{net,TIR,cf}}$) atmospheric conditions:

$$\text{CRE}_{\text{sol}} = F_{\text{net,sol,cld}} - F_{\text{net,sol,cf}}, \tag{3}$$

$$\text{CRE}_{\text{TIR}} = F_{\text{net,TIR,cld}} - F_{\text{net,TIR,cf}}. \tag{4}$$

The sum of CRE_{sol} and CRE_{TIR} gives the total CRE (CRE_{tot}). It depends on both, microphysical (e. g., cloud phase; liquid water path, LWP; and effective radius, r_{eff}) and macrophysical (e. g., cloud fraction; cloud height) cloud properties, but also on the thermodynamic circumstances, the solar zenith angle (SZA), and the surface albedo (Shupe and Intrieri, 2004).

In contrast to the cooling effect of clouds on global average (Allan, 2011), long-term, ground-based observations at single locations around the Arctic identified an average warming effect of clouds at the surface, ranging from $3.5\,\text{W}\,\text{m}^{-2}$ to $33\,\text{W}\,\text{m}^{-2}$ (Dong et al., 2010; Intrieri et al., 2002; Miller et al., 2015; Ebell et al., 2020). While the warming effect of CRE_{TIR} dominates for the frequently occurring, relatively warm low-level clouds that are typically related to distinct temperature inversions, the cooling effect of CRE_{sol} is limited by the high surface albedo and SZA (during polar day) characteristic for the Arctic (e. g., Curry et al., 1996; Shupe and Intrieri, 2004). During summer, however, the relatively low SZA causes the solar cooling effect to dominate over the TIR warming effect (Ebell et al., 2020; Dong et al., 2010; Intrieri et al., 2002), which determines a seasonal cycle of the CRE. Spatial differences of the environmental conditions among the measurement sites mainly cause

---

[1] The terms "solar" and "thermal-infrared" are often referred to as "shortwave" and "longwave". However, since the latter terms might be relative, we use the former terms throughout this manuscript (Bohren and Clothiaux, 2006, page 22f.)

the variability of the surface CRE found in the literature. For example, the average $\mathrm{CRE_{tot}}$ observed during the Surface HEat Budget of the Arctic Ocean (SHEBA) drift experiment (Intrieri et al., 2002), or on the Greenland ice sheet (Summit, Miller et al., 2015), where the surface was covered by snow or ice all year round, is larger compared to the partly snow-free land surfaces at Barrow (Dong et al., 2010) or Ny-Ålesund (Ebell et al., 2020).

The comparison of the different CRE results is further hampered by the inconsistent consideration of the cloud impact on the thermodynamic profiles and on the surface albedo (Stapf et al., 2021a, 2020). Some studies applied the radiative-transfer approach, where the cloud-free state is simulated by only removing the cloud, neglecting adjustments of the thermodynamic profiles and the surface albedo between cloudy and cloud-free conditions (e. g., Intrieri et al., 2002). Others determined the CRE from measurements only, which were obtained during cloudy and cloud-free conditions (e. g., Dong et al., 2010). This measurement-based approach accounts for the adjustment effects (Stapf et al., 2020). The resulting differences between the two approaches can be significant. Stapf et al. (2021a) demonstrated that, due to the decreased surface temperature, $\mathrm{CRE_{TIR}}$ obtained during SHEBA would be up to $25\,\mathrm{W\,m^{-2}}$ weaker in autumn if the measurement-based approach was used. In summer, no significant differences were found. Since the temporal dependence of the thermodynamic adjustments to cloud dissipation complicates an accurate and continuous quantification of this effect (Walsh and Chapman, 1998; Wendisch et al., 2022b), differences between both approaches will remain and likely depend on cloud type, season, and surface conditions. In contrast, the conceptual differences resulting from the cloud-induced surface albedo change can be reduced for the radiative-transfer approach. For snow-covered surfaces, Stapf et al. (2020) applied an albedo parameterization to obtain the surface albedo in cloud-free conditions and found a doubling of $\mathrm{CRE_{sol}}$ in the Fram Strait at the beginning of the melting season when the retrieved albedo was used for the calculation of the cloud-free net irradiance.

The majority of previous CRE studies in the Arctic as well as the investigations of the cloud impact on the surface albedo and the CRE (Stapf et al., 2020) were conducted over sea ice or mostly snow-covered surfaces. Less attention has been paid to the CRE over open (ice-free) ocean (Kay et al., 2016), although this situation will become more dominant in the future Arctic. Over an open ocean, quite different characteristics of the mean CRE and the cloud impact on the surface albedo appear. However, measurements of the REB and the CRE are difficult to obtain over open ocean. Shipborne radiation measurements mostly consist of the downward irradiances only and rely on assumptions or complementary (e. g., satellite) measurements of surface albedo, near-surface air temperature, and surface emissivity to calculate the upward irradiances (Protat et al., 2017; Barrientos-Velasco et al., 2022). Polavarapu (1978) obtained the net irradiance from a combination of two pairs of radiometers, which were mounted at the left and right outsides of the ship's structure and shadowed at the half facing towards the ship. Kay and L'Ecuyer (2013) used satellite observations to derive the surface CRE and found an annual mean $\mathrm{CRE_{tot}}$ similar to that from Ebell et al. (2020). This similarity likely results from the observation of snow-covered and snow-free surfaces in both studies, while most other aforementioned studies only investigated snow-covered surfaces

To characterize the surface CRE over the individual sea ice and open ocean surfaces in close proximity to each other, this study uses airborne measurements of broadband downward and upward irradiances combined with radiative transfer simulations. For this purpose, the data from three airborne campaigns performed during different seasons are analyzed. Section 2 introduces the measurements as well as the campaigns and their surface and meteorological characteristics. The radiative

Table 1. Statistical overview of the analyzed campaigns.

Campaign	AFLUX	ACLOUD	MOSAiC-ACA
Period	19 March–11 April 2019	23 May–26 June 2017	30 August–13 September 2020
Aircraft	*Polar 5*	*Polar 5*, *Polar 6*	*Polar 5*
Total flight hours	67.5	178.5	44.3
Low-level flight hours	6.1	13.6	1.5
Observations over sea ice (%)	65	50	2
Observations over open ocean (%)	16	15	72
Observations over the MIZ (%)	19	35	26
Median SZA (°)	76	60	76

transfer simulations and the effect of the cloud-induced albedo change over open ocean are described in Sect. 3. CRE_{sol} and CRE_{TIR} as well as their variability as a function of the surface type, and between the different campaigns are assessed in Sect. 4. Conclusions are given in Sect. 5.

2 Observations

2.1 Airborne campaigns and instrumentation

To study atmospheric processes in the lower Arctic troposphere, three airborne campaigns were deployed to collect measurements of cloud, surface, and thermodynamic properties during different seasons near Svalbard. The Airborne measurements of radiative and turbulent FLUXes of energy and momentum in the Arctic boundary layer (AFLUX) campaign was conducted in early spring 2019 (Mech et al., 2022), while the Arctic CLoud Observations Using airborne measurements during polar Day (ACLOUD) campaign was performed in late spring/early summer 2017 (Wendisch et al., 2019). Additionally, the Multidisciplinary drifting Observatory for the Study of Arctic Climate – Airborne observations in the Central Arctic (MOSAiC-ACA) campaign was conducted in late summer 2020 and accompanied the MOSAiC drift expedition with airborne measurements (Shupe et al., 2022). Table 1 lists the periods during which the campaigns were deployed. During ACLOUD, the measurements were accomplished onboard the two research aircraft *Polar 5* and *Polar 6* from Alfred Wegener Institute, Helmholtz Centre for Polar and Marine Research (Wesche et al., 2016). During the other campaigns, only *Polar 5* was operated. The majority of the observations took place in the eastern Fram Strait north-west of Svalbard, the corresponding flight tracks are displayed in Fig. 1. Depending on the campaign, between 5 % and 20 % of the total flight time was dedicated to low-level flight sections, not exceeding a flight altitude of 250 m.
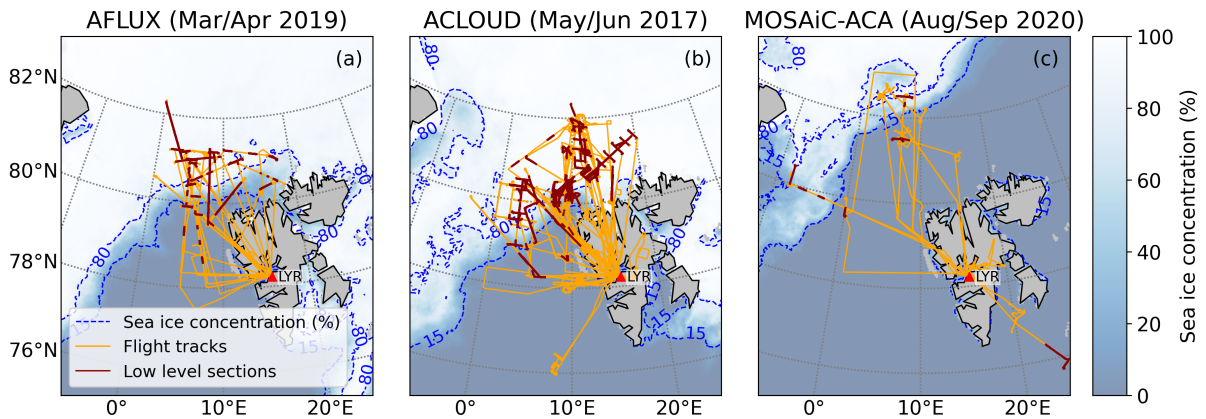
Figure 1. Flight tracks (orange) and low-level sections (dark-red) performed during (a) AFLUX, (b) ACLOUD, and (c) MOSAiC-ACA based at Longyearbyen (LYR). Each panel shows the mean sea ice concentration f_{ice} (derived from space-borne observations, Spreen et al., 2008) present during the respective campaign, the dashed blue lines indicate the 15 % and 80 % isolines of f_{ice} that confine the MIZ according to the definition of Strong and Rigor (2013).

During the low-level sections, the broadband irradiances $F_{sol}^{\downarrow}$ and $F_{sol}^{\uparrow}$ on the one hand, and $F_{TIR}^{\downarrow}$ and $F_{TIR}^{\uparrow}$ on the other hand were measured by pairs of upward- and downward-directed pyranometers (sensitive in the solar range between 0.2–3.6 μm) and pyrgeometers (sensitive in the TIR range between 4.5–42 μm) and recorded at a frequency of 20 Hz. An inertia correction was applied, which enables to resolve fluctuations in the order of 2 s and to remove the inertia-induced time shift of the time series (Ehrlich and Wendisch, 2015). Furthermore, the impact of the aircraft attitude on $F_{sol}^{\downarrow}$ was accounted for by a common correction method (Bannehr and Schwiesow, 1993). Because of remaining uncertainties in the estimation of the fraction of direct solar irradiance, the irradiance data for aircraft attitude angles exceeding 5° in roll and pitch angle were discarded. From the broadband irradiance measurements, $F_{net,sol,cld}$ and $F_{net,TIR,cld}$ (Eqs. 1 and 2), and the surface albedo (ratio of $F_{sol}^{\uparrow}$ and $F_{sol}^{\downarrow}$) in mostly cloudy conditions were derived. The exclusion of data due to the aircraft attitude and severe icing of the instruments, led to a reduction of the low-level data set by 41 %, 63 %, and 44 % for AFLUX, ACLOUD, and MOSAiC-ACA, respectively. The remaining low-level flight time used for the analysis is given in Table 1.

Although the measurements were not performed directly at the surface, the impact of the atmosphere below the aircraft is small if no cloud or fog layers are present there. For a flight altitude of 100 m, radiative transfer simulations for different cloud and albedo properties revealed an underestimation of less than 1.3 W m^{-2} for CRE$_{sol}$ and an overestimation of of less than 1.25 W m^{-2} for CRE$_{TIR}$ compared to the surface. Larger differences are expected for the occasionally occurring sea smoke below the aircraft. However, the analysis focuses on the radiative effect of clouds above the flight altitude, i. e., neglecting the sea smoke. Only in case of indirect effects (e. g., change of the measured albedo by the sea smoke), its influence is discussed in the remainder of this study.

Additionally, the sea ice concentration f_{ice} was derived from measurements of a three-channel digital camera equipped with a 180° fish-eye lens (sampling frequency: one image every 6 seconds). The individual pixels of the radiance-calibrated

images of the fish-eye camera were classified into the different surface types based on their reflection characteristics (Becker et al., 2022), in order to derive the cosine-weighted surface type fraction of each image. Based on the transmissivity of the

130   clouds, which is the fraction of the downward irradiances measured in mostly cloudy atmospheric conditions and simulated for cloud-free conditions, an equivalent LWP was retrieved using the method of Stapf et al. (2020) and assuming clouds with a droplet r_{eff} of 8 µm. Despite the neglected cloud ice and the fixed r_{eff} in the retrieval, the equivalent LWP provides a robust estimate of the optical thickness of the clouds. Regular profiles of temperature and relative humidity were obtained using the in situ meteorological measurements during aircraft ascents and descents, sondes dropped from the aircraft, and, for the

135   higher atmosphere, radiosoundings launched at Ny-Ålesund. Measurements of profiles of the cloud liquid water content (LWC) obtained from various in situ cloud probes were used to retrieve cloud boundaries. Further details on the aircraft instrumentation and data processing are provided by Ehrlich et al. (2019b) and Mech et al. (2022).

2.2   Sea ice situation during the campaigns

The different distributions of sea ice in the Fram Strait region during the three campaigns investigated in this paper are depicted

140   in Fig. 1 based on the space-borne observations of f_{ice} (Spreen et al., 2008). While the sea ice edge was roughly located between 80–81° N during AFLUX (Fig. 1a), it was situated slightly further south during ACLOUD (Fig. 1b). During both campaigns, the region east of Svalbard was covered by almost closed sea ice. Since MOSAiC-ACA was performed temporally close to the annual sea ice minimum, ice-free conditions were present east of the island and the sea ice edge in the Fram Strait was mostly north of 82° N. It was reached by *Polar 5* only for a short flight section (Fig. 1c). Consequently, more than half of the low-level

145   observations during AFLUX and ACLOUD were performed over closed sea ice, while during MOSAiC-ACA, the fraction of observations over sea ice amounts to only 2 % and strongly limits the statistical representation of this situation. Instead, almost three quarters of the low-level observations were performed over open ocean during MOSAiC-ACA compared to about 15 % during the other campaigns (Table 1). Note that for the low-level observations, the MIZ comprises all observations with f_{ice} between 0.05 and 0.95 and, thus, deviates from the MIZ definition of Strong and Rigor (2013), where f_{ice} is between 0.15 and

150   0.8. These modified thresholds are motivated by the strong impact of the surface type on the surface radiative properties, which significantly changes already for small fractions of sea ice or open ocean and requires a more rigorous separation of the MIZ (e. g., Becker et al., 2022).

2.3   Thermodynamic profiles and cloud base height

Mean profiles of various thermodynamic properties measured during the campaigns are shown in Figs. 2a and 2b. According

155   to the time of the year, AFLUX showed significantly colder temperatures compared to the remaining campaigns (Fig. 2a). While the mean near-surface temperature over sea ice was −16 °C during AFLUX, it was around −3 °C during ACLOUD and MOSAiC-ACA. The near-surface temperature over open ocean was close to the freezing point during ACLOUD and MOSAiC-ACA, and below −10 °C during AFLUX. Over sea ice, a surface-based temperature inversion was present during all campaigns, which was strongest during AFLUX. In contrast, temperature inversions were weak or absent over open ocean,
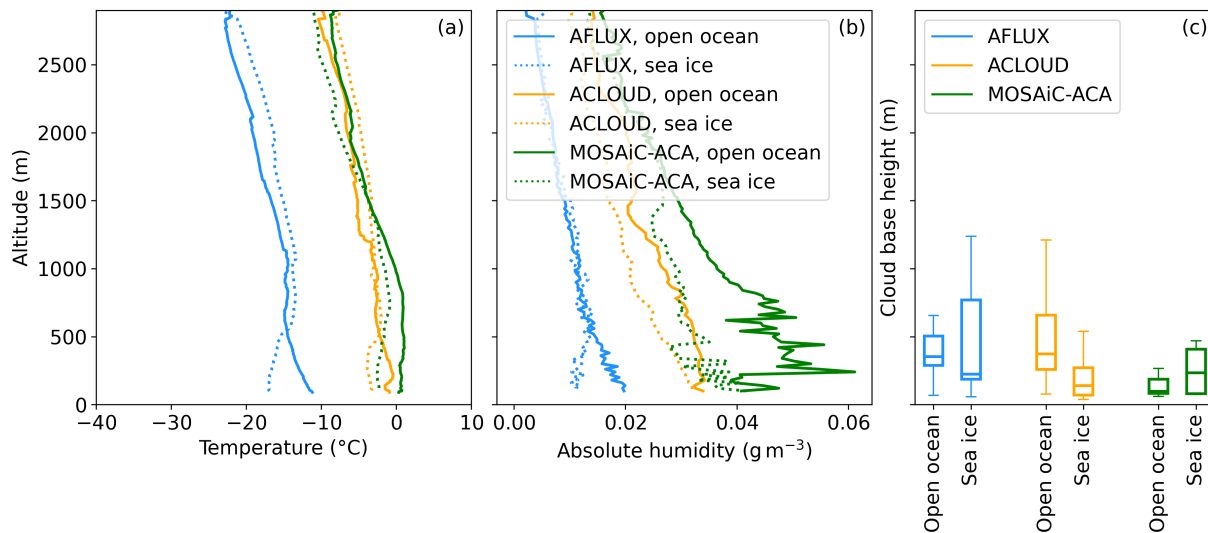
Figure 2. Mean profiles of (a) temperature, and (b) absolute humidity obtained during aircraft ascents and descents of the individual campaigns (colour-coded), separated for the different surface types (linestyle-coded). (c) Box-whisker plots of the cloud base height obtained from the in situ cloud probes (see text for details). The surface type separation is based on the space-borne observations of f_{ice} (Spreen et al., 2008) and the surface type definition of Strong and Rigor (2013).

with the least stable mean profile obtained for AFLUX. In higher altitudes, the mean profiles over sea ice and open ocean of the same campaign agreed well.

The emission and absorption by the atmospheric water vapour relevant for the surface $F_{\mathrm{net,TIR}}$, depends on the absolute humidity (AH), which is shown in Fig. 2b. Due to the lower equilibrium pressure and the resulting lower concentration of water vapour for colder temperatures, AFLUX showed the lowest AH. The differently shaped temperature profiles over sea ice and open ocean below 500 m are imprinted in the mean AH profile. Despite the comparable temperature range, the AH was significantly lower during ACLOUD than during MOSAiC-ACA, which is due to the lower relative humidity (RH, not shown). Furthermore, the lower RH over sea ice reduced the AH compared to open ocean during ACLOUD. During MOSAiC-ACA, both the higher temperature and the larger RH caused the increased AH over open ocean below 1500 m.

The surface $\mathrm{CRE_{TIR}}$ largely depends on the cloud base temperature, which is determined by the location of the cloud within the temperature profile. Figure 2c shows statistics of the cloud base height obtained from the in situ cloud probes. Clouds were identified by a LWC threshold of $0.005\,\mathrm{g\,cm^{-3}}$. During AFLUX, the median cloud base height over open ocean was 352 m. Over sea ice, the median cloud base height was lower (223 m) but more variable. The typical cloud base temperature range is estimated from the mean temperature (Fig. 2a) in the altitudes corresponding to the inter-quartile range (IQR) of the cloud base height. For AFLUX, the cloud base temperature was in the range of $-14\,°\mathrm{C}$ over sea ice, and between $-13\,°\mathrm{C}$ and $-17\,°\mathrm{C}$ over open ocean. During ACLOUD, the median cloud base height of 372 m over open ocean was similar compared to AFLUX, while clouds over sea ice were significantly lower (140 m). The resulting cloud base temperatures range around -3–$0\,°\mathrm{C}$ and
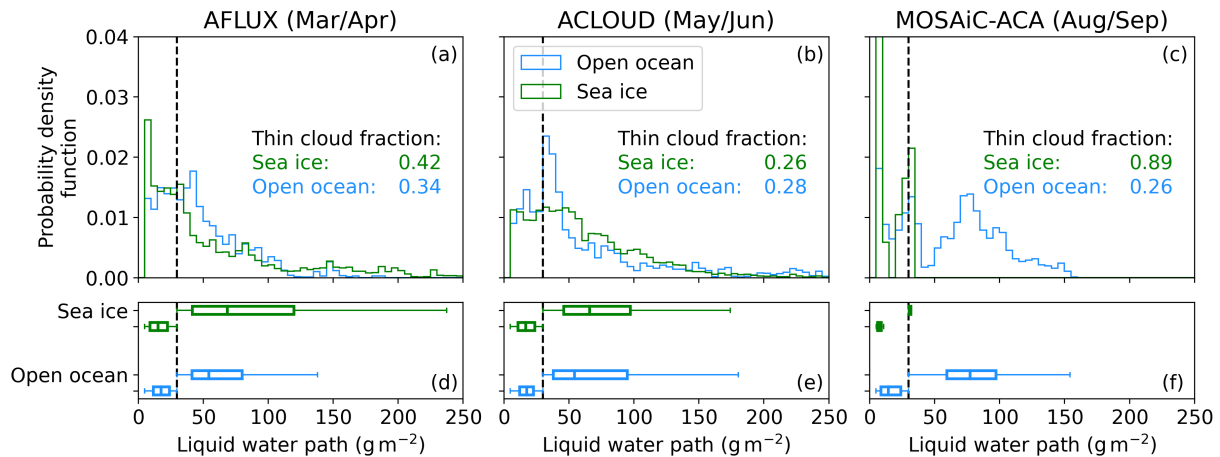
Figure 3. Probability density function of the equivalent LWP over sea ice and open ocean (colour-coded) for (a) AFLUX, (b) ACLOUD, and (c) MOSAiC-ACA. Only observations classified as cloudy (equivalent LWP $> 5\,\mathrm{g\,m^{-2}}$) were considered. The vertical dashed lines located at $30\,\mathrm{g\,m^{-2}}$ indicate the threshold used for the separation of thin and thick clouds. The numbers in (a–c) represent the fraction of observations with thin clouds with respect to the total amount of cloudy observations. (d–f) Box-whisker plots of the equivalent LWP separating thin (left boxplots) and thick clouds (right boxplots).

$-3\,°\mathrm{C}$ over open ocean and sea ice, respectively. During MOSAiC-ACA, the median cloud base height over sea ice was $234\,\mathrm{m}$, while clouds over open ocean showed very low bases ($97\,\mathrm{m}$). The cloud base temperatures were about $0\,°\mathrm{C}$ and $-2\,°\mathrm{C}$ over open ocean and sea ice, respectively. In general, the slightly colder cloud base temperatures over sea ice seem to rather result from the colder low-level temperatures than from the different cloud base heights.

2.4 Cloud liquid water path

The statistical characteristics of the equivalent cloud LWP assembled during the campaigns are illustrated in Fig. 3 as a rough measure for optical thickness. During AFLUX (Fig. 3a), clouds with an equivalent LWP below $10\,\mathrm{g\,m^{-2}}$ were most frequent over sea ice, while the largest mode of equivalent LWP over open ocean occurs between $30\,\mathrm{g\,m^{-2}}$ and $50\,\mathrm{g\,m^{-2}}$. $\mathrm{CRE_{TIR}}$ is especially sensitive to the LWP of optically thin clouds below $30\,\mathrm{g\,m^{-2}}$ (e. g., Shupe and Intrieri, 2004; Ebell et al., 2020), but almost constant for larger LWPs. Accordingly, this threshold was used to distinguish between thin and thick clouds, which are analyzed separately. Corresponding to the PDFs, the median equivalent LWP of thin clouds is lower over sea ice than over open ocean, with values of $15\,\mathrm{g\,m^{-2}}$ and $18\,\mathrm{g\,m^{-2}}$, respectively (Fig. 3d). In contrast, the median of thick clouds is larger over sea ice. However, thin clouds occurred more frequently over sea ice compared to open ocean (numbers in Fig. 3a).

The PDF of the equivalent LWP derived from ACLOUD measurements (Fig. 3b) reveals a similar distribution of thin clouds over sea ice and open ocean. Both surface types showed similar median values for thin clouds (around $17\,\mathrm{g\,m^{-2}}$, Fig. 3e). Over open ocean, clouds with an equivalent LWP of 30–$50\,\mathrm{g\,m^{-2}}$ were most common, while larger LWPs were more frequent over sea ice than over open ocean. Thus, the median equivalent LWP of thick clouds was larger over sea ice. The thin cloud fraction

was slightly lower over sea ice compared to open ocean. Compared to AFLUX, thin clouds occurred significantly less frequent over both surface types.

During MOSAiC-ACA (Fig. 3c), the vast majority of the clouds over the sparsely sampled sea ice showed an extremely low equivalent LWP. The median equivalent LWP of thin clouds was $7\,\mathrm{g\,m^{-2}}$ (Fig. 3f) and almost $90\,\%$ of the sampled clouds were thin. These observations are statistically not representative and very likely don't reflect typical conditions present over sea ice during this season. In contrast, the equivalent LWP of clouds over open ocean showed a broader distribution with a strong mode of thick clouds. The thin cloud fraction over open ocean was similar to the one observed during ACLOUD. Compared to the other campaigns, the median of the equivalent LWP of thin clouds over open ocean was slightly lower and amounted to $14\,\mathrm{g\,m^{-2}}$.

3 Simulation of the net irradiance in assumed cloud-free conditions

3.1 Radiative transfer simulations

Section 2.1 describes the measurements of $F_{\mathrm{net,sol,cld}}$ (in mostly cloudy conditions) and $F_{\mathrm{net,TIR,cld}}$. To calculate both $\mathrm{CRE_{sol}}$ and $\mathrm{CRE_{TIR}}$, $F_{\mathrm{net,sol,cf}}$ and $F_{\mathrm{net,TIR,cf}}$ need to be simulated. For this purpose, the one-dimensional radiative transfer solver DISORT is applied (Stamnes et al., 1988), which is embedded in the library for radiative transfer *libRadtran* (Emde et al., 2016). The radiative transfer simulations were performed using the method proposed by Stapf et al. (2020). For both spectral ranges, the atmospheric state was obtained from thermodynamic profiles measured during ascents or descents adjacent to the respective low level-section, which were topped by the temporally closest radiosounding. Aerosol properties were not considered in the simulations. In addition to these settings, $F_{\mathrm{net,TIR,cf}}$ was simulated using a surface emissivity of 0.99 for snow (Warren, 1982), which is similar for open ocean at least for the atmospheric window (8–$13\,\mu\mathrm{m}$) region (Konda et al., 1994). Instead of the surface emissivity, the simulation of $F_{\mathrm{net,sol,cf}}$ additionally requires the SZA and the definition of the local surface albedo in cloud-free conditions, which is different from the surface albedo measured in cloudy conditions. From the simulations, the direct/diffuse fraction of $F_{\mathrm{sol}}^{\downarrow}$ was obtained for cloud-free conditions.

3.2 Impact of clouds on the surface albedo

3.2.1 Surface albedo over open ocean in cloud-free and cloudy conditions

While Stapf et al. (2020) analyzed the impact of clouds on the surface albedo of sea ice, the following analysis focuses on similar effects influencing the surface albedo of open ocean. The change of the broadband albedo due to the presence of clouds is a result of two effects: First, the changing amount of direct and diffuse solar radiation (geometry effect), and, second, the changing spectral distribution of the downward solar irradiance (spectral weighting effect). In general, the broadband surface albedo α is given by

$$\alpha = \frac{F_{\mathrm{sol}}^{\uparrow}}{F_{\mathrm{sol}}^{\downarrow}} = \frac{\int_{\mathrm{sol}} F_{\lambda}^{\uparrow}(\lambda)\,\mathrm{d}\lambda}{\int_{\mathrm{sol}} F_{\lambda}^{\downarrow}(\lambda)\,\mathrm{d}\lambda}. \tag{5}$$

$F^\uparrow_{\mathrm{sol}}$ and $F^\downarrow_{\mathrm{sol}}$ are obtained by integrating the spectral upward and downward irradiances, $F^\uparrow_\lambda$ and $F^\downarrow_\lambda$, over the wavelengths λ of the solar range (indicated by $\int_{\mathrm{sol}}$). To introduce the spectral albedo α_λ, $F^\uparrow_\lambda$ is replaced by $F^\downarrow_\lambda$ and α_λ:

$$
\alpha = \int_{\mathrm{sol}} \alpha_\lambda(\lambda) \cdot \frac{F^\downarrow_\lambda(\lambda)}{\int_{\mathrm{sol}} F^\downarrow_\lambda(\lambda)\,\mathrm{d}\lambda}\,\mathrm{d}\lambda. \tag{6}
$$

Equation 6 shows that the broadband albedo represents a weighted average depending on α_λ and $F^\downarrow_\lambda$, which serves as a weight function. While α_λ changes due to the geometry effect, a change of the normalized weight function w, with

$$
w = \frac{F^\downarrow_\lambda(\lambda)}{\int_{\mathrm{sol}} F^\downarrow_\lambda(\lambda)\,\mathrm{d}\lambda}, \tag{7}
$$

describes the spectral weighting effect. Both effects are analyzed in the following.

α_λ and w over open ocean were simulated with *libRadtran*, applying a parameterization of the directional reflection of open ocean surfaces with varying SZA and wind speed in 10 m altitude (Cox and Munk, 1954). To illustrate the effect of clouds on the surface albedo, simulations containing boundary layer clouds (400–600 m) with variable LWP and a fixed r_{eff} of 8 μm were performed.

The change of α_λ due to different illumination geometries is shown in Fig. 4a. In cloud-free conditions, α_λ is dominated by the reflection of the direct component of $F^\downarrow_\lambda$. Beside their different patterns, α_λ is significantly larger for a SZA of 75°, which is representative for AFLUX and MOSAiC-ACA, compared to a SZA of 60°, representative for ACLOUD. The almost constant α_λ above 1000 nm is 0.20 for 75°, but only 0.07 for 60°. This difference is due to the enhanced specular reflection at the air–water interface for larger incident angles (i. e., SZA), according to Fresnel's equations. In cloudy conditions (LWP of 80 g m^{-2}), α_λ is modified by the predominating diffuse illumination and reveals slightly lower values compared to the cloud-free case with a SZA of 60°. The best agreement between α_λ in cloudy and cloud-free conditions was found for a SZA of 52° (not shown), which can be referred to as an effective incident zenith angle in cloudy conditions. Thus, the geometry effect causes a lower surface albedo in cloudy conditions compared to cloud-free conditions for SZAs typical for the Arctic, with a larger difference for larger SZAs. Due to a reduction of specular reflection on a roughened surface, this difference decreases as the wind speed is increased, especially for large SZAs (Jin et al., 2004).

The broadband albedo is also affected by the spectral distribution of the incident irradiance (Eq. 6), which is described by w and can be modified by clouds. Spectra of w corresponding to the cases discussed above are illustrated in Fig. 4b. At visible wavelengths (e. g., 500 nm), w is larger in cloudy conditions compared to cloud-free conditions, while the situation is reversed in the near-infrared (NIR) range (e. g., 1600 nm) due to enhanced absorption by cloud particles. Consequently, α_λ in the visible wavelength range, which is slightly higher compared to α_λ in the NIR range, contributes more strongly to the broadband albedo in cloudy conditions than it does in the cloud-free case. This spectral weighting partly counteracts the spectral albedo geometry effect on the broadband albedo.
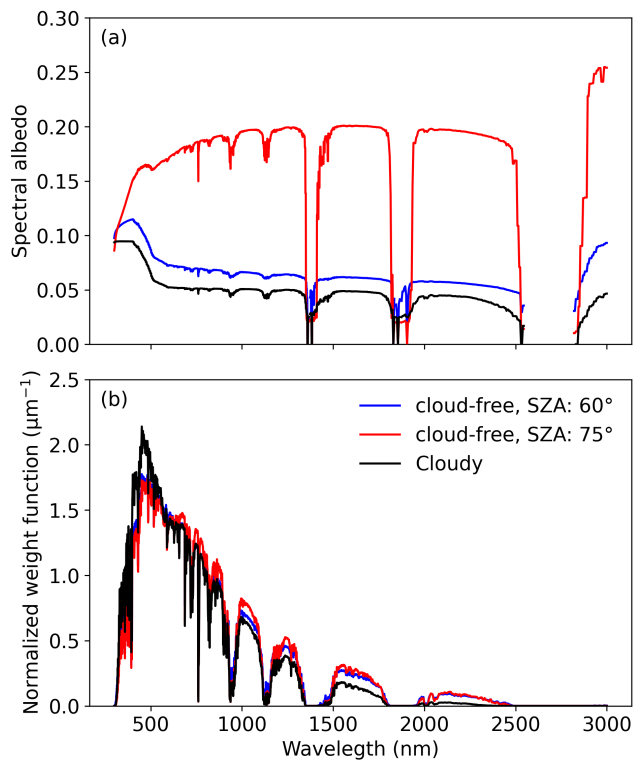
Figure 4. (a) Simulations of the spectral surface albedo α_λ of open ocean for two different SZAs in cloud-free conditions, and for cloudy conditions (LWP of $80\,\mathrm{g\,m^{-2}}$, independent of SZA). (b) Simulations of the spectral normalized weight functions w for the same scenarios. The wind speed of $1\,\mathrm{m\,s^{-1}}$ represents a calm surface.

3.2.2 Parameterization of the open ocean and sea ice albedo in cloud-free conditions

To account for the cloud-induced change of the surface albedo in the calculation of the cloud-free net irradiance, parameteriza-
tions are used to retrieve the surface albedo in cloud-free conditions. The sea ice albedo is retrieved using the method described
by Stapf et al. (2020), which is based on the parameterization of Gardner and Sharp (2010). This parameterization depends on
the SZA, the equivalent cloud LWP, and the specific surface area (SSA) of snow, which is a measure for the snow grain size and
was retrieved from the measured surface albedo. For open ocean, the parameterization of Jin et al. (2011) was used to obtain
the surface albedo in cloud-free conditions. The required input include the SZA, the wind speed measured in flight altitude and
scaled down to $10\,\mathrm{m}$ using the logarithmic wind profile with a roughness length of $2{\cdot}10^{-4}\,\mathrm{m}$ (offshore conditions), and the
simulated fraction of diffuse incident radiation in cloud-free conditions (Sect. 3.1). For a mixture of open ocean and sea ice,
the parameterized albedos of both surface types are linearly combined using f_ice obtained from the fish-eye camera (Becker
et al., 2022).

Figure 5 illustrates the parameterized broadband albedo as a function of the LWP. The broadband open ocean albedo (Fig. 5a)
decreases with increasing LWP, which indicates that the geometry effect dominates over the spectral weighting effect. This is
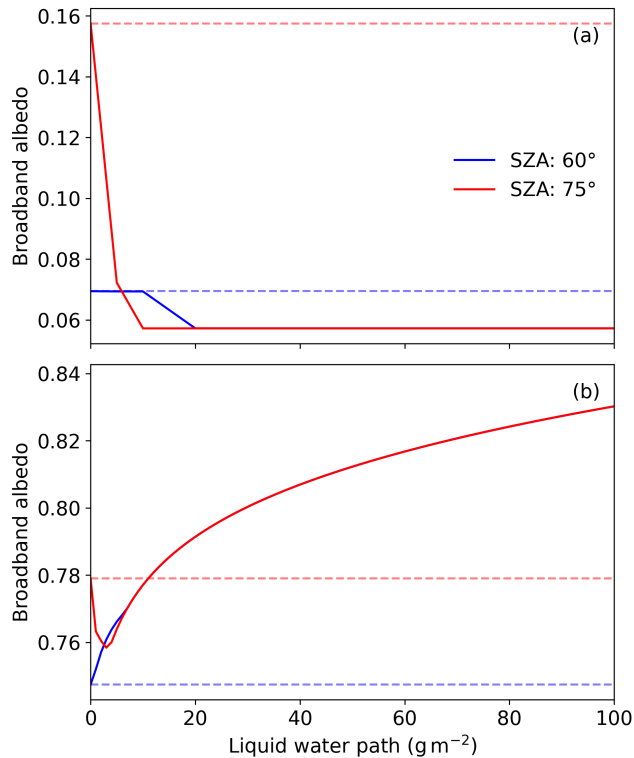
Figure 5. Broadband albedo of (a) open ocean, and (b) sea ice as a function of the cloud LWP for different SZAs. The open ocean albedo is based on the parameterization of Jin et al. (2011) with a $10\,\mathrm{m}$ wind speed of $1\,\mathrm{m\,s^{-1}}$. The sea ice albedo is based on the parameterization of Gardner and Sharp (2010) with a SSA of $80\,\mathrm{m^2\,kg^{-1}}$. The attenuated dashed lines represent the respective cloud-free surface albedos.

due to the relatively low spectral differences of the open ocean α_λ (Fig. 4a). Similar to α_λ, the broadband open ocean albedo in diffuse conditions (LWPs larger than $20\,\mathrm{g\,m^{-2}}$) is independent of the SZA and converges at 0.06, while the albedo in cloud-free conditions increases for increasing SZA. Thus, the cloud-free albedo is only slightly larger than the diffuse albedo for a SZA of $60°$, but reaches 0.16 for a SZA of $75°$. For larger wind speeds, the difference between the cloudy and cloud-free albedos
270 decreases (not shown).

In contrast to open ocean, α_λ of snow-covered sea ice shows large discrepancies, with high values in the visible and low values in the NIR range (e. g., Stapf et al., 2020, their Fig. 3). Thus, the spectral weighting effect becomes more dominant and leads to an increase of the broadband albedo with increasing LWP (Fig. 5b). While this is true for the entire LWP range for a SZA of $60°$, a slight albedo decrease is observed for the lowest LWPs and a SZA of $75°$. This feature arises from the geometry
275 effect surpassing the spectral weighting effect for optically thin clouds when the Sun is low enough. The cloud-free albedo is 0.75 and 0.78 for SZAs of $60°$ and $75°$, respectively. Similar to open ocean, the surface albedo of sea ice does not differ with SZA in diffuse conditions. Consequently, the albedo differences between cloudy and cloud-free conditions are larger for lower SZAs within the typical LWP range.
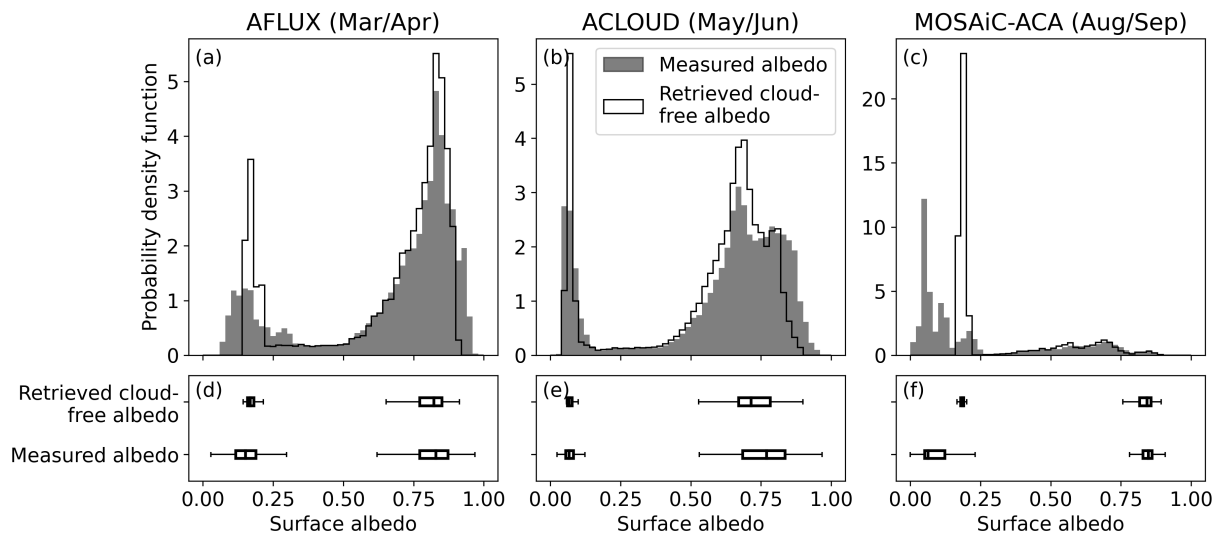
Figure 6. Probability density function of the surface albedos measured in mostly cloudy conditions (shadings) and retrieved for cloud-free conditions (lines) for (a) AFLUX, (b) ACLOUD, and (c) MOSAiC-ACA. (d–f) Box-whisker plots of the retrieved cloud-free and measured surface albedo separated for open ocean (left boxplots) and sea ice (right boxplots).

To retrieve the cloud-free surface albedo from the mostly cloudy albedo measurements performed during the low-level
280 sections, the surface albedo parameterizations were applied to the measurements of the three campaigns. Figure 6 illustrates the effect of the cloud-induced albedo change by comparing the frequency distributions of the measured (mostly cloudy) and retrieved (cloud-free) surface albedos. The left and the right mode of all distributions correspond to the open ocean and sea ice surfaces, respectively. Compared to the measured albedo, the distribution of the retrieved cloud-free albedo is narrowed over open ocean during AFLUX (Figs. 6a, 6d). Although a notably higher open ocean albedo would be expected in cloud-
285 free conditions for SZAs present during AFLUX (Fig. 5a), the measured and retrieved median albedo values of 0.15 and 0.17, respectively, did not differ significantly. This is probably due to the frequently occurring sea smoke between the aircraft and the ocean surface, which artificially increased the measured albedo compared to the expected values (Fig. 5a). For the snow-covered sea ice, the median values of 0.83 and 0.82 indicate only small differences between the measured albedo and the retrieved cloud-free albedo, which is in accordance with Fig. 5b for the typical SZA range during AFLUX. Similarly, no
290 significant difference between measured and retrieved cloud-free albedo of open ocean could be observed during ACLOUD (Figs. 6b, 6e). However, as suggested by Fig. 5b, a significant albedo shift over sea ice is obvious for ACLOUD, where the median of the surface albedo decreased from 0.77 in the observed cloudy conditions to 0.71 for the retrieved cloud-free albedo. In general, the observations during ACLOUD are characterized by a lower sea ice albedo compared to AFLUX, which is due to the onset of the melting season. Despite the similar SZA range, the cloud-induced change of the open ocean albedo
295 showed different effects for AFLUX and MOSAiC-ACA. The median of the measured albedo was only 0.06 during the latter (Figs. 6c, 6f). However, the median retrieved cloud-free albedo of 0.19 was similar to the value retrieved for AFLUX. The
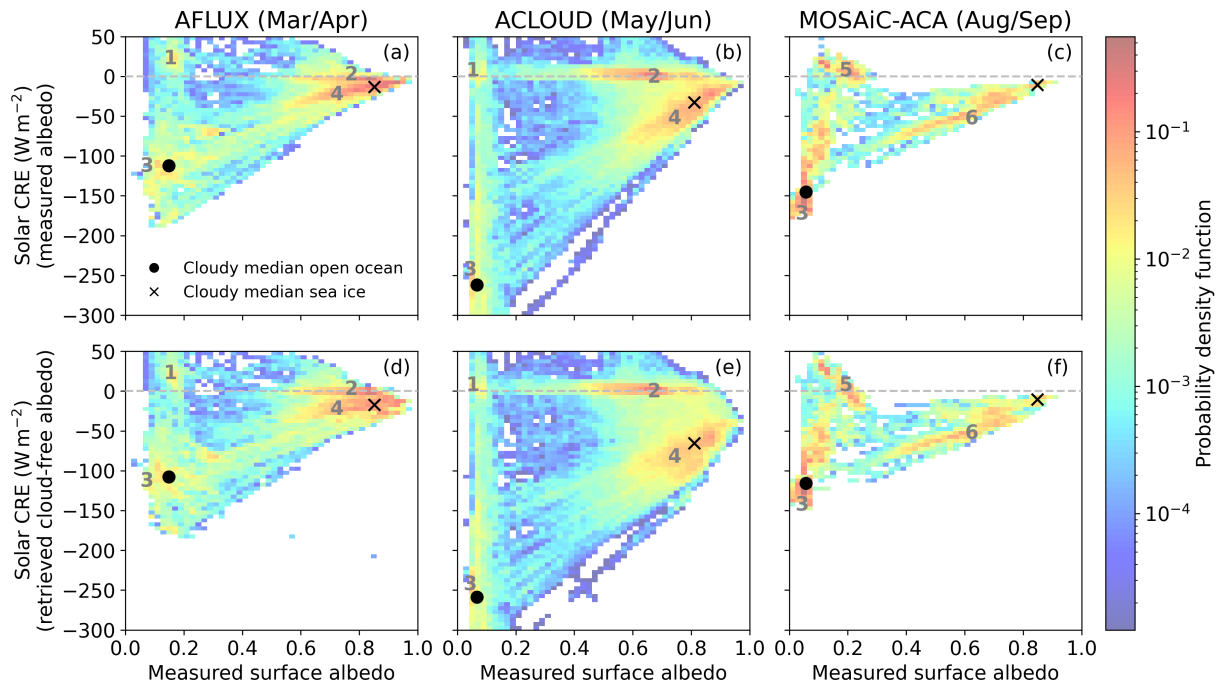
Figure 7. Two-dimensional probability density function of CRE_{sol} and the measured (mostly cloudy) surface albedo (as an indicator for the surface type) for AFLUX (a,d), ACLOUD (b,e), and MOSAiC-ACA (c,f). The upper row (a–c) shows the distributions of CRE_{sol} neglecting the cloud-induced change of the surface albedo, while this effect is included in the lower row (d–f). The horizontal dashed lines mark a CRE_{sol} of $0\,W\,m^{-2}$. The symbols represent the median of CRE_{sol} and the measured surface albedo over the surface types given in the legend in (a) and only considering cloudy observations (equivalent $LWP > 5\,g\,m^{-2}$). The numbered modes represent (1) cloud-free open ocean, (2) cloud-free sea ice, (3) cloudy open ocean, (4) cloudy sea ice, (5) thin/broken clouds, and (6) cloudy MIZ conditions.

rarely sampled sea ice during MOSAiC-ACA is only expressed by the rightmost, very small mode. Similar to AFLUX, the sea ice albedo did not change significantly between cloudy and cloud-free conditions. The mode located roughly between 0.25 and 0.75 represents observations over the MIZ.

4 Cloud radiative effect

4.1 Solar cloud radiative effect

The variability of CRE_{sol} at the surface during the three campaigns is assessed by analyzing the frequency distributions of CRE_{sol} as a function of the strongly influential measured surface albedo, which are shown in Fig. 7. To quantify the impact of the cloud-induced albedo change on CRE_{sol}, two distributions are presented for each campaign. While the cloud-induced surface albedo change is neglected in Figs. 7a–7c, Figs. 7d–7f show CRE_{sol} corrected for this effect. For AFLUX and ACLOUD, the distributions of Fig. 7 reveal four distinct modes (indicated by the numbers 1–4). The modes 1 and 2 are

located around or slightly above $0\,\mathrm{W\,m^{-2}}$ and reflect mainly cloud-free conditions, while the remaining modes (modes 3 and 4) indicate the cooling effect of clouds in the solar range. Through their distinct surface albedos, $\mathrm{CRE_{sol}}$ over open ocean (mode 3) and sea ice (mode 4) surfaces are clearly distinct. During MOSAiC-ACA (Figs. 7c, 7f), thin or broken clouds (mode 5) and frequent observations over the MIZ in cloudy conditions (mode 6) altered the mode structure.

The comparison of the two distributions per campaign exposes the shift of several modes due to the cloud-induced albedo change. For AFLUX (Figs. 7a, 7d), only minor changes can be observed, which is in accordance with the similar distributions of measured and retrieved (cloud-free) surface albedo (Fig. 6a). The albedo change increased (reduced) the median $\mathrm{CRE_{sol}}$ over open ocean (sea ice) by $4\,\mathrm{W\,m^{-2}}$. The artificial absence of a larger $\mathrm{CRE_{sol}}$ increase over open ocean is due to the sea smoke and the resulting too high measured surface albedo discussed in Sect. 3.2.2. The actual change of $\mathrm{CRE_{sol}}$ remains unclear. As discussed by Stapf et al. (2020), the increased albedo of sea ice in cloudy conditions caused a significant shift of mode 4 during ACLOUD (Figs. 7b, 7e) and almost doubled the median of the uncorrected $\mathrm{CRE_{sol}}$ of $-33\,\mathrm{W\,m^{-2}}$. In contrast, $\mathrm{CRE_{sol}}$ over open ocean was hardly affected. During MOSAiC-ACA, the weakening of the solar cooling effect due to the increased open ocean albedo in cloud-free conditions (Fig. 6c) is expressed by the shift of mode 3 (Figs. 7c, 7f). The median of the uncorrected $\mathrm{CRE_{sol}}$ ($-145\,\mathrm{W\,m^{-2}}$) imposed an artifact of $29\,\mathrm{W\,m^{-2}}$ cooling due to the neglect of the cloud-induced albedo change. The sea ice–dominated MIZ (mode 6) is not affected by the albedo change, because the negligible increase of the sea ice albedo and the more significant decrease of the open ocean albedo towards cloud-free conditions cancel.

Using $\mathrm{CRE_{sol}}$ accounting for the cloud-induced albedo change (Figs. 7d–7f), the features of the individual distributions and the differences among them are discussed in the following. For AFLUX (Fig. 7d), mode 1 over open ocean shows a remarkably positive $\mathrm{CRE_{sol}}$ with a median of $20\,\mathrm{W\,m^{-2}}$ for an equivalent LWP of less than $5\,\mathrm{g\,m^{-2}}$. This solar warming effect is due to broken cumulus clouds, which often enhance $F_{\mathrm{sol}}^{\downarrow}$ compared to a cloud-free situation for several minutes by scattering additional solar radiation towards the surface (cloud enhancement, Mol et al., 2023). Broken clouds frequently occur during cold air outbreaks over open ocean, when the cold air advected over the warm ocean reduces the thermodynamic stability and leads to the formation of cloud streets (e. g., Brümmer, 1996). Thus, mode 1 combines cloud-free situations with broken cloud observations, the latter producing a low retrieved equivalent LWP that is indistinguishable from cloud-free conditions. Due to the high surface albedo of sea ice (larger than 0.6), the magnitude of $\mathrm{CRE_{sol}}$ was small over this surface type (mode 4, median of $-17\,\mathrm{W\,m^{-2}}$, black cross in Fig. 7d) and could be hardly distinguished from the absent $\mathrm{CRE_{sol}}$ in cloud-free conditions (mode 2), especially for very bright scenes. In contrast, the low open ocean albedo enabled a much stronger solar cooling effect of the clouds (mode 3) with a median $\mathrm{CRE_{sol}}$ of $-108\,\mathrm{W\,m^{-2}}$ (black dot in Fig. 7d).

The $\mathrm{CRE_{sol}}$ distribution of ACLOUD (Fig. 7e) is shaped more clearly compared to AFLUX due to the better statistics of the data. $\mathrm{CRE_{sol}}$ over open ocean and sea ice (modes 3 and 4) reveals median values of $-259\,\mathrm{W\,m^{-2}}$ and $-65\,\mathrm{W\,m^{-2}}$, respectively, which indicates a significantly stronger solar cooling effect compared to AFLUX. Although the lower surface albedo contributed to this stronger cooling effect during ACLOUD, a normalization of $\mathrm{CRE_{sol}}$ with the cosine of the SZA (not shown) reveals that the major contribution to the $\mathrm{CRE_{sol}}$ differences between the two campaigns resulted from the different solar illumination as a consequence of the clearly distinct SZA ranges (Table 1). Note that the SZA exhibits not only an annual,

but also a daily cycle. However, since most of the flights were conducted around solar noon, the SZA variability within one campaign was small.

The observations from MOSAiC-ACA reveal a large variability and a relatively unclear mode structure (Fig. 7f), which is due to the much less significant statistics compared to the other campaigns (see Table 1). Modes 1 and 2 are missing in the distribution, since cloud-free conditions were not sampled during MOSAiC-ACA. Instead of mode 1, mode 5 represents broken or very thin clouds over open ocean. Similar to AFLUX, this mode peaks at positive CRE_{sol} values due to the broken cloud effect. However, in contrast to AFLUX, also negative CRE_{sol} values were observed, probably resulting from rather overcast thin cloud conditions. Due to the similar Sun elevation (Table 1), the median of CRE_{sol} over open ocean ($-116\,\mathrm{W\,m^{-2}}$, mode 3) was similar compared to AFLUX. In contrast to the other campaigns, the rare observations over homogeneous sea ice during MOSAiC-ACA are not reflected in an own mode. These observations are rather included in the cloudy MIZ mode (mode 6), which expands to albedo values of down to 0.4.

The present analysis indicates a significant variability of CRE_{sol} between the campaigns and the underlying surface types. In accordance with previous studies (e. g., Intrieri et al., 2002; Miller et al., 2015), CRE_{sol} between the campaigns mostly varied due to the seasonally changing SZA, with a stronger cooling effect for a decreasing SZA. The differences between open ocean and sea ice are a result of their distinct surface albedos. The impact of clouds on the surface albedo affects CRE_{sol} differently, depending on surface type and SZA. While the albedo in cloudy conditions and the solar cooling effect of clouds over sea ice are mostly enhanced for relatively low Arctic SZAs, larger SZAs rather weaken the cooling effect over open ocean. Given the seasonality of the sea ice extent in the Fram Strait region (Fig. 1), this effect rather stengthens the cooling effect during early summer and weakens it during late summer. The resulting convergence of the affected cloudy modes during ACLOUD and MOSAiC-ACA (Fig. 7) suggests a weaker amplitude of the seasonal cycle of CRE_{sol} considering the cloud-induced albedo modifications.

4.2 Thermal-infrared cloud radiative effect

CRE_{TIR} is determined by a complex interplay of the environmental thermodynamics, and the cloud macrophysical and microphysical properties. The frequency distributions of CRE_{TIR} for all three campaigns are depicted in Fig. 8, separated for sea ice and open ocean. Independent of the underlying surface type, the distributions of CRE_{TIR} during AFLUX (Figs. 8a, 8d) and ACLOUD (Figs. 8b, 8e) reveal two distinct modes. Similar to CRE_{sol}, the mode located around $0\,\mathrm{W\,m^{-2}}$ represents cloud-free conditions, while the second mode clearly indicates the warming effect of the clouds in the TIR range. In contrast to CRE_{sol}, the order of magnitude of CRE_{TIR} does not differ between the surface types because the surface temperature does not affect CRE_{TIR}. Differences result only from the influence of the surface on the cloud and thermodynamic properties.

The median CRE_{TIR} observed in cloudy conditions during AFLUX was $67\,\mathrm{W\,m^{-2}}$ over open ocean and $64\,\mathrm{W\,m^{-2}}$ over sea ice. The slightly lower value for the latter was caused by the enhanced frequency of observations with relatively low CRE_{TIR} ($< 30\,\mathrm{W\,m^{-2}}$), which might be linked to the larger fraction of thin clouds (Fig. 3a) or to the slightly lower cloud base temperature (Fig. 2) over sea ice. For AFLUX, a cloud base temperature change of 1 K results in a change of the CRE_{TIR} in the order of $4\,\mathrm{W\,m^{-2}}$, which is approximately the difference between the median CRE_{TIR} over sea ice and open ocean.
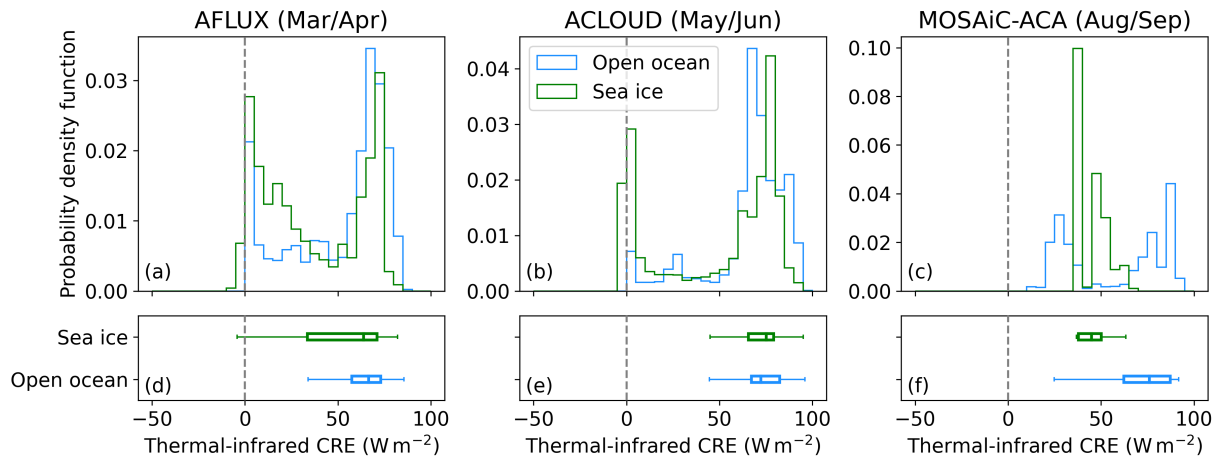
Figure 8. Probability density function of CRE_{TIR} for (a) AFLUX, (b) ACLOUD, and (c) MOSAiC-ACA, separated for sea ice and open ocean (colour-coded). (d–f) Box-whisker plots of CRE_{TIR} only considering cloudy observations (equivalent $LWP > 5\,g\,m^{-2}$). The vertical dashed lines mark a CRE_{TIR} of $0\,W\,m^{-2}$. Note that, due to a lack of the corresponding observations, none of the modes in (c) represents actual cloud-free conditions. The thinnest clouds, however, revealed an equivalent $LWP < 5\,g\,m^{-2}$ and did, thus, not contribute to the statistics shown in (f).

375   During ACLOUD (Figs. 8b, 8e), cloud-free conditions were significantly less frequent over open ocean than over sea ice. Instead, the distribution of open ocean reveals an additional small mode around $25\,W\,m^{-2}$. CRE_{TIR} in cloudy conditions did not differ significantly between the surface types with median values ranging between $72\,W\,m^{-2}$ over open ocean and $75\,W\,m^{-2}$ over sea ice. The slightly stronger CRE_{TIR} over sea ice cannot be explained by the cloud base temperature (Fig. 2), which showed lower values over sea ice. Likely, the more frequent occurrence of thick clouds (Fig. 3b) caused this tendency.

380   Also compared to AFLUX, the thicker clouds during ACLOUD are likely the reason for the stronger CRE_{TIR}, since the increased absolute humidity counteracts the effect of the higher cloud base temperature during ACLOUD (Cox et al., 2015). Except the additional small mode for open ocean, the cloud-free and cloudy modes are more clearly separated during ACLOUD compared to AFLUX.

      Similar to the CRE_{sol}, the low amount of data obtained during MOSAiC-ACA results in a less significant mode structure

385 (Figs. 8e, 8f). Only in the distribution of open ocean, two distinct modes are visible. Due to the lack of cloud-free observations, the mode with the smallest CRE_{TIR} represents the broken cloud conditions (around $25\,W\,m^{-2}$). However, these observations mostly coincide with an equivalent LWP of less than $5\,g\,m^{-2}$ and do not significantly contribute to the median CRE_{TIR} of $75\,W\,m^{-2}$ in cloudy conditions over open ocean. This median value is similar to the median CRE_{TIR} obtained during ACLOUD, which is probably due to the similar frequency of thick clouds (Fig. 3). Over sea ice, a significantly weaker CRE_{TIR}

390 was observed during MOSAiC-ACA ($45\,W\,m^{-2}$), which results from the limited sampling statistics. Nevertheless, this is in agreement with the lower observed cloud base temperature (Fig. 2) and the significantly thinner clouds (Fig. 3c).
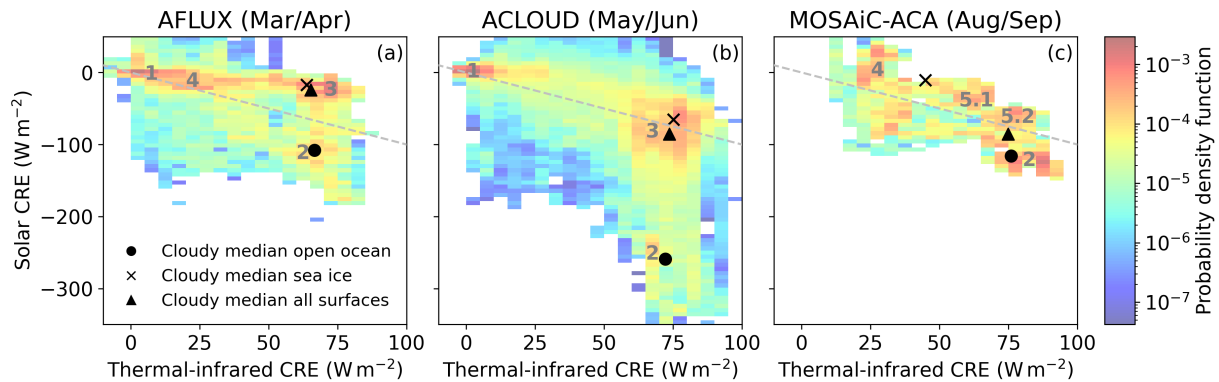
Figure 9. Two-dimensional probability density function of CRE_{sol} and CRE_{TIR} for (a) AFLUX , (b) ACLOUD, and (c) MOSAiC-ACA. The diagonal dashed lines represent the $0\,W\,m^{-2}$ isoline of CRE_{tot}. The symbols represent the median of CRE_{sol} and CRE_{TIR} over the surface types given in the legend in (a) and only considering cloudy observations (equivalent $LWP > 5\,g\,m^{-2}$). The numbered modes represent (1) cloud-free, (2) cloudy open ocean, (3) cloudy sea ice, (4) thin/broken clouds, and (5.1/5.2) cloudy MIZ conditions.

4.3 Total cloud radiative effect

The previous analysis showed that the variability of CRE_{TIR} between the campaigns and the surface types is significantly lower than the variability of CRE_{sol}. Thus, the latter is the major driver of the variability of CRE_{tot}. Depending on whether the solar cooling or the TIR warming effect dominates, CRE_{tot} determines whether a cloud has a cooling or a warming effect on the surface. Figure 9 illustrates two-dimensional frequency distributions combining CRE_{sol} and CRE_{TIR} to assess CRE_{tot}. All modes visible in Fig. 9 can be attributed to the modes discussed in Figs. 7 and 8. In the distributions of AFLUX (Fig. 9a) and ACLOUD (Fig. 9b), mode 1 is clustered around $0\,W\,m^{-2}$ for both CRE_{sol} and CRE_{TIR} and combines the mostly cloud-free observations over open ocean and sea ice. The clearly distinct CRE_{sol} over the different surface types (Fig. 7) separates the cloudy modes over open ocean (mode 2, stronger solar cooling effect) and sea ice (mode 3), while CRE_{TIR} is similar.

Over open ocean (mode 2), clouds of sufficient LWP showed a total cooling effect (negative CRE_{tot}, values below the dashed line in Fig. 9) during all campaigns. However, the magnitudes of CRE_{tot} differed significantly as quantified by the median values of $-48\,W\,m^{-2}$, $-185\,W\,m^{-2}$, and $-36\,W\,m^{-2}$ during AFLUX, ACLOUD, and MOSAiC-ACA, respectively. Due to the lower SZA during ACLOUD, the solar cooling effect dominated CRE_{tot}. Over sea ice, the TIR warming effect was dominant over the solar cooling effect during AFLUX, resulting in a median CRE_{tot} of $42\,W\,m^{-2}$. During ACLOUD, however, CRE_{sol} and CRE_{TIR} roughly compensated, leading to a small median CRE_{tot} of $7\,W\,m^{-2}$.

During AFLUX, a significant amount of observations ranges in a transition between modes 1 and 3. These data correspond to the observations over sea ice with low CRE_{TIR} that were already discussed in Fig. 8a. The clouds during these situations were rather thin with a median equivalent LWP of $19\,g\,m^{-2}$ compared to $54\,g\,m^{-2}$ for the observations forming the cloudy sea ice mode (mode 3). The almost absent solar cooling in combination with a TIR warming leads to the total warming effect

of these thin clouds often discussed in literature (e. g., Miller et al., 2015), which under certain circumstances can induce ice melting (Bennartz et al., 2013).

Again, the sparse statistics during MOSAiC-ACA need to be interpreted with caution and represent only a subsample of possible cloud conditions (Fig. 9c). Instead of the cloud-free mode (mode 1) observed for the other campaigns, mode 4 represents the broken clouds that produced only a slightly positive CRE_{sol}, but a significantly positive CRE_{TIR} with median values of $7\,W\,m^{-2}$ and $26\,W\,m^{-2}$, respectively. The resulting positive CRE_{tot} underlines that the warming effect of broken clouds can be observed also over open ocean. Modes 5.1 and 5.2 reveal a cloud warming effect over the MIZ, while a separate sea ice mode is missing.

For the regional average CRE_{tot}, the sea ice concentration within the area of observations is most relevant. While the sea ice situation in the Fram Strait north-west of Svalbard was similar during AFLUX and ACLOUD (Figs. 1a and 1b), the sea ice edge was located significantly further north during MOSAiC-ACA (Fig. 1c) and the MIZ was broader. This also affected the fraction of observations obtained for each of the surface types and determined the strength of the different modes in Fig. 9. As a proxy for the entire Fram Strait, the median of CRE_{tot} observed in cloudy conditions during one single campaign was calculated regardless of surface type (triangles in Fig. 9). For MOSAiC-ACA, this median CRE_{tot} of $-27\,W\,m^{-2}$ was close to the median for open ocean due to the dominance of this surface type. During AFLUX, a positive median CRE_{tot} of $25\,W\,m^{-2}$, and during ACLOUD, a negative median CRE_{tot} of $-16\,W\,m^{-2}$ was observed, both ranging close to median values of sea ice. Given the different SZA ranges during both campaigns, this indicates that clouds over the Fram Strait showed a warming effect at the surface during AFLUX (spring) and an almost neutral to slightly negative CRE_{tot} during ACLOUD (early summer). MOSAiC-ACA revealed a similar median of CRE_{tot} compared to AFLUX for the individual surface types. However, the dominant open ocean surfaces during MOSAiC-ACA caused the clouds to have an average cooling effect during late summer.

5   Conclusions

To compare the warming or cooling effects of clouds over sea ice and open ocean during different times of the year, the surface CRE was evaluated from observations performed during three campaigns in the Fram Strait north-west of Svalbard. The campaigns AFLUX, ACLOUD, and MOSAiC-ACA were characterized by significantly different sea ice coverages and thermodynamic states during spring, early summer, and late summer, respectively. The CRE was calculated from a combination of airborne broadband radiation measurements and radiative transfer simulations. While $F_{net,sol,cld}$ and $F_{net,TIR,cld}$ were measured during low-level flight sections, the corresponding $F_{net,sol,cf}$ and $F_{net,TIR,cf}$ were simulated and accounted for changes of the surface albedo between cloudy and cloud-free conditions (Stapf et al., 2020). This was done by retrieving the cloud-free surface albedo from parameterizations for sea ice and open ocean surfaces. The radiative impact of clouds on the surface albedo differed between the surface types and was not uniform among the different campaigns.

CRE_{sol} and CRE_{tot} were affected distinctly by these cloud-induced differences of the surface albedo, mainly depending on the SZA. The consideration of this effect almost doubled CRE_{sol} over sea ice during ACLOUD, as already discussed by Stapf et al. (2020). In contrast, the larger SZAs present during the other campaigns suppressed similar changes of CRE_{sol}. However,

over open ocean, the impact of the cloud-induced albedo change increases with increasing SZA. Thus, the solar cooling effect over open ocean was weakened by about 20 % during MOSAiC-ACA, while ACLOUD was not affected. During AFLUX, the albedo change was masked by the presence of sea smoke.

$\mathrm{CRE_{sol}}$ strongly varied between sea ice and open ocean surfaces as well as among the campaigns. While the low surface albedo caused a strong solar cooling effect over open ocean, the cooling effect over sea ice was rather weak and partly not distinguishable from cloud-free conditions. This weak cooling was often supported by the presence of thin clouds. Due to the lower SZA, $\mathrm{CRE_{sol}}$ showed a significantly stronger cooling effect during ACLOUD compared to the other campaigns.

The variability of $\mathrm{CRE_{TIR}}$ results from a complex interplay between changing thermodynamic and cloud properties. In contrast to $\mathrm{CRE_{sol}}$, $\mathrm{CRE_{TIR}}$ varied only weakly between the surface types and the campaigns and mostly showed median values between $64\,\mathrm{W\,m^{-2}}$ and $76\,\mathrm{W\,m^{-2}}$. Compared to the other campaigns, a weaker $\mathrm{CRE_{TIR}}$ was found during AFLUX, which was caused by the enhanced frequency of optically thin clouds.

The variability of $\mathrm{CRE_{tot}}$ is driven by $\mathrm{CRE_{sol}}$. A negative $\mathrm{CRE_{tot}}$, dominated by the solar cooling effect, was found over open ocean during all campaigns. This cooling effect was strongest during ACLOUD ($-185\,\mathrm{W\,m^{-2}}$) compared to the other two campaigns (around $-40\,\mathrm{W\,m^{-2}}$). Over sea ice and the MIZ, the warming effect of $\mathrm{CRE_{TIR}}$ clearly dominated during AFLUX ($42\,\mathrm{W\,m^{-2}}$) and MOSAiC-ACA ($22\,\mathrm{W\,m^{-2}}$), while $\mathrm{CRE_{sol}}$ and $\mathrm{CRE_{TIR}}$ roughly compensated during ACLOUD. Broken and optically thin clouds showed a total warming effect, independent of the underlying surface. This is due to their almost neutral to slightly positive $\mathrm{CRE_{sol}}$ and their significantly positive $\mathrm{CRE_{TIR}}$. In addition to the SZA, $\mathrm{CRE_{tot}}$ not separated for the surface types differs between the campaigns due to the seasonally different sea ice distributions. For each campaign, the sea ice distribution in the Fram Strait region is imprinted in the fraction of observations over the respective surface types. The high fraction of observations over sea ice during AFLUX and ACLOUD implies a warming and almost neutral effect of clouds in the Fram Strait during spring and early summer, respectively. In contrast, the frequent observations over open ocean during MOSAiC-ACA cause a cooling effect of clouds in the Fram Strait during late summer.

The short low-level flight segments during the campaigns are not necessarily representative for an entire season from a climatological point of view. The results might be biased by the flight strategy and the spatial and temporal selection of low-level sections to satisfy different campaign goals. Furthermore, not all synoptic conditions could be captured due to weather-caused flight limitations. To overcome these limitations and to improve the statistics of the surface CRE, extensive low-level sections are necessary regardless of the weather conditions. However, various CRE differences between the campaigns could be attributed to their seasonality. Although observations of annual cycles of the CRE over sea ice are available (e. g., SHEBA, MOSAiC), the lack of long-term observations over open ocean complicates a robust characterization of the CRE. This especially holds since ice-free conditions will likely become more dominant in the future Arctic. The validation of satellite CRE retrievals with airborne measurements might be the key for long-term observations of the CRE over open ocean. This study and the published datasets of the CRE in the Fram Strait (Stapf et al., 2021c; Becker et al., 2023) could provide a basis for such investigations and for further research of cloud-related processes and feedback mechanisms in numerical models. Nevertheless, the predominant cooling effect of clouds over open ocean will likely lead to a negative contribution to further warming in the Arctic.

Data availability. All data analyzed in this manuscript are published on the PANGAEA database. The broadband irradiance and KT19 data can be found at Stapf et al. (2019, https://doi.pangaea.de/10.1594/PANGAEA.900442, ACLOUD), Stapf et al. (2021b, https://doi.pangaea.de/10.1594/PANGAEA.932020, AFLUX), and Becker et al. (2021b, https://doi.pangaea.de/10.1594/PANGAEA.936232, MOSAiC-ACA). The meteorological measurements (temperature, RH, wind speed) during the flights were published by Hartmann et al. (2019, https://doi.pangaea.de/10.1594/PANGAEA.902849, ACLOUD), Lüpkes et al. (2022, https://doi.pangaea.de/10.1594/PANGAEA.945844, AFLUX), and Hartmann et al. (2022, https://doi.pangaea.de/10.1594/PANGAEA.947787, MOSAiC-ACA). Dropsonde measurements were provided by Ehrlich et al. (2019a, https://doi.pangaea.de/10.1594/PANGAEA.900204, ACLOUD), Becker et al. (2020, https://doi.pangaea.de/10.1594/PANGAEA.921996, AFLUX), and Becker et al. (2021a, https://doi.pangaea.de/10.1594/PANGAEA.933581, MOSAiC-ACA), while the radiosounding are available at Maturilli (2020, https://doi.pangaea.de/10.1594/PANGAEA.914973). The microphysical cloud properties obtained from the in situ cloud probes can be found at Dupuy et al. (2019, https://doi.pangaea.de/10.1594/PANGAEA.899074, ACLOUD), Moser and Voigt (2022, https://doi.pangaea.de/10.1594/PANGAEA.940564, AFLUX), and Moser et al. (2022, https://doi.pangaea.de/10.1594/PANGAEA.940557, MOSAiC-ACA). Datasets containing the retrieved sea ice fraction, equivalent LWP, cloud-free albedo, and CRE were published by Stapf et al. (2021c, https://doi.pangaea.de/10.1594/PANGAEA.932010, ACLOUD and AFLUX) and Becker et al. (2023, https://doi.pangaea.de/10.1594/PANGAEA.957759, MOSAiC-ACA).

Author contributions. All authors contributed to the discussion of the results and the editing of the article. SB drafted the article, analyzed the data, and performed the ocean albedo analysis. MW and AE designed the experimental basis of this study.

Competing interests. The authors declare that they have no conflict of interest.

Acknowledgements. We gratefully acknowledge the funding by the Deutsche Forschungsgemeinschaft (DFG, German Research Foundation) – Projektnummer 268020496 – TRR 172, within the Transregional Collaborative Research Center "ArctiC Amplification: Climate Relevant Atmospheric and SurfaCe Processes, and Feedback Mechanisms (AC)[3]. This work was carried out and data used in this article were produced as part of the international Multidisciplinary drifting Observatory for the Study of Arctic Climate (MOSAiC) with the tag MOSAiC20192020 during the Airborne observations in the Central Arctic (MOSAiC-ACA, P5-221_MOSAiC_ACA_2020). We thank AWI logistics department, the crews of the research aircraft Polar 5 and 6 and all persons involved in the expedition of the Research Vessel Polarstern during MOSAiC (AWI_PS122_00) as listed in Nixdorf et al. (2021). This work was funded by the Open Access Publishing Fund of Leipzig University supported by the DFG within the program Open Access Publication Funding.

References

505 Allan, R. P.: Combining satellite data and models to estimate cloud radiative effect at the surface and in the atmosphere, Meteorol. Appl., 18, 324–333, https://doi.org/10.1002/met.285, 2011.

Bannehr, L. and Schwiesow, R.: A Technique to Account for the Misalignment of Pyranometers Installed on Aircraft, J. Atmos.Ocean. Tech., 10, 774–777, https://doi.org/10.1175/1520-0426(1993)010<0774:attaft>2.0.co;2, 1993.

Barrientos-Velasco, C., Deneke, H., Hünerbein, A., Griesche, H. J., Seifert, P., and Macke, A.: Radiative closure and cloud effects on the
510 radiation budget based on satellite and shipborne observations during the Arctic summer research cruise, PS106, Atmos. Chem. Phys., 22, 9313–9348, https://doi.org/10.5194/acp-22-9313-2022, 2022.

Becker, S., Ehrlich, A., Stapf, J., Lüpkes, C., Mech, M., Crewell, S., and Wendisch, M.: Meteorological measurements by dropsondes released from POLAR 5 during AFLUX 2019, PANGAEA, https://doi.org/10.1594/PANGAEA.921996, 2020.

Becker, S., Ehrlich, A., Mech, M., Lüpkes, C., and Wendisch, M.: Meteorological measurements by dropsondes released from POLAR 5
515 during MOSAiC-ACA 2020, PANGAEA, https://doi.org/10.1594/PANGAEA.933581, 2021a.

Becker, S., Stapf, J., Ehrlich, A., and Wendisch, M.: Aircraft measurements of broadband irradiance during the MOSAiC-ACA campaign in 2020, PANGAEA, https://doi.org/10.1594/PANGAEA.936232, 2021b.

Becker, S., Ehrlich, A., Jäkel, E., Carlsen, T., Schäfer, M., and Wendisch, M.: Airborne measurements of directional reflectivity over the Arctic marginal sea ice zone, Atmos. Meas. Tech., 15, 2939–2953, https://doi.org/10.5194/amt-15-2939-2022, 2022.

520 Becker, S., Ehrlich, A., Schäfer, M., and Wendisch, M.: Cloud radiative forcing, LWP and cloud-free albedo derived from airborne broadband irradiance observations during the MOSAiC-ACA campaign, PANGAEA, https://doi.org/10.1594/PANGAEA.957759, 2023.

Bennartz, R., Shupe, M. D., Turner, D. D., Walden, V. P., Steffen, K., Cox, C. J., Kulie, M. S., Miller, N. B., and Pettersen, C.: July 2012 Greenland melt extent enhanced by low-level liquid clouds, Nature, 496, 83–86, https://doi.org/10.1038/nature12002, 2013.

Bohren, C. F. and Clothiaux, E. E.: Fundamentals of Atmospheric Radiation – An Introduction with 400 Problems, Wiley-VCH Verlag,
525 Weinheim, Germany, 2006.

Brümmer, B.: Boundary-layer modification in wintertime cold-air outbreaks from the Arctic sea ice, Bound.-Lay. Meteorol., 80, 109–125, https://doi.org/10.1007/bf00119014, 1996.

Ceppi, P., Hartmann, D. L., and Webb, M. J.: Mechanisms of the Negative Shortwave Cloud Feedback in Middle to High Latitudes, J. Clim., 29, 139–157, https://doi.org/10.1175/jcli-d-15-0327.1, 2015.

530 Choi, Y.-S., Hwang, J., Ok, J., Park, D.-S. R., Su, H., Jiang, J. H., Huang, L., and Limpasuvan, T.: Effect of Arctic clouds on the ice-albedo feedback in midsummer, Int. J. Climatol., 40, 4707–4714, https://doi.org/10.1002/joc.6469, 2020.

Cox, C. and Munk, W.: Measurement of the Roughness of the Sea Surface from Photographs of the Sun's Glitter, J. Opt. Soc. Am., 44, 838–850, https://doi.org/10.1364/josa.44.000838, 1954.

Cox, C. J., Walden, V. P., Rowe, P. M., and Shupe, M. D.: Humidity trends imply increased sensitivity to clouds in a warming Arctic, Nat.
535 Commun., 6, https://doi.org/10.1038/ncomms10117, 2015.

Curry, J. A., Schramm, J. L., Rossow, W. B., and Randall, D.: Overview of Arctic Cloud and Radiation Characteristics, J. Clim., 9, 1731–1764, https://doi.org/10.1175/1520-0442(1996)009<1731:OOACAR>2.0.CO;2, 1996.

Dong, X., Xi, B., Crosby, K., Long, C. N., Stone, R. S., and Shupe, M. D.: A 10 year climatology of Arctic cloud fraction and radiative forcing at Barrow, Alaska, J. Geophys. Res., 115, https://doi.org/10.1029/2009jd013489, 2010.

540 Dupuy, R., Jourdan, O., Mioche, G., Gourbeyre, C., Leroy, D., and Schwarzenböck, A.: CDP, CIP and PIP In-situ arctic cloud microphysical properties observed during ACLOUD-AC3 campaign in June 2017, PANGAEA, https://doi.org/10.1594/PANGAEA.899074, 2019.

Ebell, K., Nomokonova, T., Maturilli, M., and Ritter, C.: Radiative Effect of Clouds at Ny-Ålesund, Svalbard, as Inferred from Ground-Based Remote Sensing Observations, J. Appl. Meteorol. Climatol., 59, 3–22, https://doi.org/10.1175/jamc-d-19-0080.1, 2020.

Ehrlich, A. and Wendisch, M.: Reconstruction of high-resolution time series from slow-response broadband terrestrial irradiance measure-
545 ments by deconvolution, Atmos. Meas. Tech., 8, 3671–3684, https://doi.org/10.5194/amt-8-3671-2015, 2015.

Ehrlich, A., Stapf, J., Lüpkes, C., Mech, M., Crewell, S., and Wendisch, M.: Meteorological measurements by dropsondes released from POLAR 5 during ACLOUD 2017, PANGAEA, https://doi.org/10.1594/PANGAEA.900204, 2019a.

Ehrlich, A., Wendisch, M., Lüpkes, C., Buschmann, M., Bozem, H., Chechin, D., Clemen, H.-C., Dupuy, R., Eppers, O., Hartmann, J., Herber, A., Jäkel, E., Järvinen, E., Jourdan, O., Kästner, U., Kliesch, L.-L., Köllner, F., Mech, M., Mertes, S., Neuber, R., Ruiz-
550 Donoso, E., Schnaiter, M., Schneider, J., Stapf, J., and Zanatta, M.: A comprehensive in situ and remote sensing data set from the Arctic CLoud Observations Using airborne measurements during polar Day (ACLOUD) campaign, Earth Syst. Sci. Data, 11, 1853–1881, https://doi.org/10.5194/essd-11-1853-2019, 2019b.

Emde, C., Buras-Schnell, R., Kylling, A., Mayer, B., Gasteiger, J., Hamann, U., Kylling, J., Richter, B., Pause, C., Dowling, T., and Bugliaro, L.: The libRadtran software package for radiative transfer calculations (version 2.0.1), Geosci. Model Dev., 9, 1647–1672,
555 https://doi.org/10.5194/gmd-9-1647-2016, 2016.

Forster, P., Storelvmo, T., Armour, K., Collins, W., Dufresne, J.-L., Frame, D., Lunt, D., Mauritsen, T., Palmer, M., Watanabe, M., Wild, M., and Zhan, H.: The Earth's Energy Budget, Climate Feedbacks, and Climate Sensitivity, in: Climate Change 2021: The Physical Science Basis. Contribution of Working Group I to the Sixth Assessment Report of the Intergovernmental Panel on Climate Change, edited by Masson-Delmotte, V., Zhai, P., Pirani, A., Connors, S., Péan, C., Berger, S., Caud, N., Chen, Y., Goldfarb, L., Gomis, M., Huang, M.,
560 Leitzell, K., Lonnoy, E., Matthews, J., Maycock, T., Waterfield, T., Yelekçi, O., Yu, R., and Zhou, B., book section 9, pp. 923—1054, Cambridge University Press, Cambridge, United Kingdom and New York, NY, USA, https://doi.org/10.1017/9781009157896.009, 2021.

Gardner, A. S. and Sharp, M. J.: A review of snow and ice albedo and the development of a new physically based broadband albedo parameterization, J. Geophys. Res., 115, https://doi.org/10.1029/2009jf001444, 2010.

Hartmann, J., Lüpkes, C., and Chechin, D.: 1Hz resolution aircraft measurements of wind and temperature during the ACLOUD campaign
565 in 2017, PANGAEA, https://doi.org/10.1594/PANGAEA.902849, 2019.

Hartmann, J., Lüpkes, C., Michaelis, J., and Herber, A.: High resolution aircraft measurements of wind and temperature during the MOSAIC-ACA campaign in 2020, PANGAEA, https://doi.org/10.1594/PANGAEA.947787, 2022.

Intrieri, J. M., Shupe, M. D., Uttal, T., and McCarthy, B. J.: An annual cycle of Arctic cloud characteristics observed by radar and lidar at SHEBA, J. Geophys. Res., 107, https://doi.org/10.1029/2000jc000423, 2002.

570 Jin, Z., Charlock, T. P., Smith, W. L., and Rutledge, K.: A parameterization of ocean surface albedo, J. Geophys. Res., 31, 26 429–26 443, https://doi.org/10.1029/2004gl021180, 2004.

Jin, Z., Qiao, Y., Wang, Y., Fang, Y., and Yi, W.: A new parameterization of spectral and broadband ocean surface albedo, Opt. Express, 19, 26 429–26 443, https://doi.org/10.1364/oe.19.026429, 2011.

Kay, J. E. and L'Ecuyer, T.: Observational constraints on Arctic Ocean clouds and radiative fluxes during the early 21st century, J. Geophys.
575 Res.: Atmos., 118, 7219–7236, https://doi.org/10.1002/jgrd.50489, 2013.

Kay, J. E., Holland, M. M., Bitz, C. M., Blanchard-Wrigglesworth, E., Gettelman, A., Conley, A., and Bailey, D.: The Influence of Local Feedbacks and Northward Heat Transport on the Equilibrium Arctic Climate Response to Increased Greenhouse Gas Forcing, Journal of Climate, 25, 5433–5450, https://doi.org/10.1175/jcli-d-11-00622.1, 2012.

Kay, J. E., L'Ecuyer, T., Chepfer, H., Loeb, N., Morrison, A., and Cesana, G.: Recent Advances in Arctic Cloud and Climate Research, Curr. Clim. Change Rep., 2, 159–169, https://doi.org/10.1007/s40641-016-0051-9, 2016.

Konda, M., Imasato, N., Nishi, K., and Toda, T.: Measurement of the sea surface emissivity, J. Oceanogr., 50, 17–30, https://doi.org/10.1007/bf02233853, 1994.

Lüpkes, C., Hartmann, J., Chechin, D., and Michaelis, J.: High resolution aircraft measurements of wind and temperature during the AFLUX campaign in 2019, PANGAEA, https://doi.org/10.1594/PANGAEA.945844, 2022.

Maturilli, M.: High resolution radiosonde measurements from station Ny-Ålesund (2017-04 et seq), PANGAEA, https://doi.org/10.1594/PANGAEA.914973, 2020.

Mech, M., Ehrlich, A., Herber, A., Lüpkes, C., Wendisch, M., Becker, S., Boose, Y., Chechin, D., Crewell, S., Dupuy, R., Gourbeyre, C., Hartmann, J., Jäkel, E., Jourdan, O., Kliesch, L.-L., Klingebiel, M., Kulla, B. S., Mioche, G., Moser, M., Risse, N., Ruiz-Donoso, E., Schäfer, M., Stapf, J., and Voigt, C.: MOSAiC-ACA and AFLUX - Arctic airborne campaigns characterizing the exit area of MOSAiC, Sci. Data, 9, https://doi.org/10.1038/s41597-022-01900-7, 2022.

Miller, N. B., Shupe, M. D., Cox, C. J., Walden, V. P., Turner, D. D., and Steffen, K.: Cloud Radiative Forcing at Summit, Greenland, Journal of Climate, 28, 6267–6280, https://doi.org/10.1175/jcli-d-15-0076.1, 2015.

Mol, W. B., van Stratum, B. J. H., Knap, W. H., and van Heerwaarden, C. C.: Reconciling Observations of Solar Irradiance Variability With Cloud Size Distributions, J. Geophys. Res.: Atmos., 128, https://doi.org/10.1029/2022jd037894, 2023.

Morrison, A. L., Kay, J. E., Frey, W. R., Chepfer, H., and Guzman, R.: Cloud Response to Arctic Sea Ice Loss and Implications for Future Feedback in the CESM1 Climate Model, J. Geophys. Res.: Atmos., 124, 1003–1020, https://doi.org/10.1029/2018jd029142, 2019.

Moser, M. and Voigt, C.: DLR in-situ cloud measurements during AFLUX Arctic airborne campaign, PANGAEA, https://doi.org/10.1594/PANGAEA.940564, 2022.

Moser, M., Voigt, C., and Hahn, V.: DLR in-situ cloud measurements during MOSAiC-ACA Arctic airborne campaign, PANGAEA, https://doi.org/10.1594/PANGAEA.940557, 2022.

Nixdorf, U., Dethloff, K., Rex, M., Shupe, M., Sommerfeld, A., Perovich, D. K., Nicolaus, M., Heuzé, C., Rabe, B., Loose, B., Damm, E., Gradinger, R., Fong, A., Maslowski, W., Rinke, A., Kwok, R., Spreen, G., Wendisch, M., Herber, A., Hirsekorn, M., Mohaupt, V., Frickenhaus, S., Immerz, A., Weiss-Tuider, K., König, B., Mengedoht, D., Regnery, J., Gerchow, P., Ransby, D., Krumpen, T., Morgenstern, A., Haas, C., Kanzow, T., Rack, F. R., Saitzev, V., Sokolov, V., Makarov, A., Schwarze, S., Wunderlich, T., Wurr, K., and Boetius, A.: MOSAiC Extended Acknowledgement, Zenodo, https://doi.org/10.5281/ZENODO.5541624, 2021.

Polavarapu, R. J.: Measurement of Net Radiation from Shipboard Sensors, J. Appl. Meteorol. (1962-1982), 17, 1062–1067, http://www.jstor.org/stable/26178571, 1978.

Protat, A., Schulz, E., Rikus, L., Sun, Z., Xiao, Y., and Keywood, M.: Shipborne observations of the radiative effect of Southern Ocean clouds, J. Geophys. Res.: Atmos., 122, 318–328, https://doi.org/10.1002/2016jd026061, 2017.

Ramanathan, V., Cess, R. D., Harrison, E. F., Minnis, P., Barkstrom, B. R., Ahmad, E., and Hartmann, D.: Cloud-Radiative Forcing and Climate: Results from the Earth Radiation Budget Experiment, Science, 243, 57–63, https://doi.org/10.1126/science.243.4887.57, 1989.

Serreze, M. C. and Barry, R. G.: Processes and impacts of Arctic amplification: A research synthesis, Global Planet. Change, 77, 85–96, https://doi.org/10.1016/j.gloplacha.2011.03.004, 2011.

Shupe, M. D. and Intrieri, J. M.: Cloud Radiative Forcing of the Arctic Surface: The Influence of Cloud Properties, Surface Albedo, and Solar Zenith Angle, J. Clim., 17, 616–628, https://doi.org/10.1175/1520-0442(2004)017<0616:crfota>2.0.co;2, 2004.

Shupe, M. D., Rex, M., Blomquist, B., Persson, P. O. G., Schmale, J., Uttal, T., Althausen, D., Angot, H., Archer, S., Bariteau, L., Beck, I., Bilberry, J., Bucci, S., Buck, C., Boyer, M., Brasseur, Z., Brooks, I. M., Calmer, R., Cassano, J., Castro, V., Chu, D., Costa, D., Cox, C. J., Creamean, J., Crewell, S., Dahlke, S., Damm, E., de Boer, G., Deckelmann, H., Dethloff, K., Dütsch, M., Ebell, K., Ehrlich, A., Ellis, J., Engelmann, R., Fong, A. A., Frey, M. M., Gallagher, M. R., Ganzeveld, L., Gradinger, R., Graeser, J., Greenamyer, V., Griesche, H., Griffiths, S., Hamilton, J., Heinemann, G., Helmig, D., Herber, A., Heuzé, C., Hofer, J., Houchens, T., Howard, D., Inoue, J., Jacobi, H.-W., Jaiser, R., Jokinen, T., Jourdan, O., Jozef, G., King, W., Kirchgaessner, A., Klingebiel, M., Krassovski, M., Krumpen, T., Lampert, A., Landing, W., Laurila, T., Lawrence, D., Lonardi, M., Loose, B., Lüpkes, C., Maahn, M., Macke, A., Maslowski, W., Marsay, C., Maturilli, M., Mech, M., Morris, S., Moser, M., Nicolaus, M., Ortega, P., Osborn, J., Pätzold, F., Perovich, D. K., Petäjä, T., Pilz, C., Pirazzini, R., Posman, K., Powers, H., Pratt, K. A., Preußer, A., Quéléver, L., Radenz, M., Rabe, B., Rinke, A., Sachs, T., Schulz, A., Siebert, H., Silva, T., Solomon, A., Sommerfeld, A., Spreen, G., Stephens, M., Stohl, A., Svensson, G., Uin, J., Viegas, J., Voigt, C., von der Gathen, P., Wehner, B., Welker, J. M., Wendisch, M., Werner, M., Xie, Z., and Yue, F.: Overview of the MOSAiC expedition: Atmosphere, Elem. Sci. Anth., 10, https://doi.org/10.1525/elementa.2021.00060, 2022.

Spreen, G., Kaleschke, L., and Heygster, G.: Sea ice remote sensing using AMSR-E 89-GHz channels, J. Geophys. Res., 113, https://doi.org/10.1029/2005jc003384, 2008.

Stamnes, K., Tsay, S.-C., Wiscombe, W., and Jayaweera, K.: Numerically stable algorithm for discrete-ordinate-method radiative transfer in multiple scattering and emitting layered media, Appl. Opt., 27, 2502–2509, https://doi.org/10.1364/ao.27.002502, 1988.

Stapf, J., Ehrlich, A., Jäkel, E., and Wendisch, M.: Aircraft measurements of broadband irradiance during the ACLOUD campaign in 2017, PANGAEA, https://doi.org/10.1594/PANGAEA.900442, 2019.

Stapf, J., Ehrlich, A., Jäkel, E., Lüpkes, C., and Wendisch, M.: Reassessment of shortwave surface cloud radiative forcing in the Arctic: consideration of surface-albedo–cloud interactions, Atmos. Chem. Phys., 20, 9895–9914, https://doi.org/10.5194/acp-20-9895-2020, 2020.

Stapf, J., Ehrlich, A., and Wendisch, M.: Influence of Thermodynamic State Changes on Surface Cloud Radiative Forcing in the Arctic: A Comparison of Two Approaches Using Data From AFLUX and SHEBA, J. Geophys. Res.: Atmos., 126, https://doi.org/10.1029/2020jd033589, 2021a.

Stapf, J., Ehrlich, A., and Wendisch, M.: Aircraft measurements of broadband irradiance during the AFLUX campaign in 2019, PANGAEA, https://doi.org/10.1594/PANGAEA.932020, 2021b.

Stapf, J., Ehrlich, A., and Wendisch, M.: Cloud radiative forcing, LWP and cloud-free albedo derived from airborne broadband irradiance observations during the AFLUX and ACLOUD campaign, PANGAEA, https://doi.org/10.1594/PANGAEA.932010, 2021c.

Strong, C. and Rigor, I. G.: Arctic marginal ice zone trending wider in summer and narrower in winter, Geophys. Res. Lett., 40, 4864–4868, https://doi.org/10.1002/grl.50928, 2013.

Walsh, J. E. and Chapman, W. L.: Arctic Cloud–Radiation–Temperature Associations in Observational Data and Atmospheric Reanalyses, J. Clim., 11, 3030–3045, https://doi.org/10.1175/1520-0442(1998)011<3030:acrtai>2.0.co;2, 1998.

Warren, S. G.: Optical properties of snow, Rev. Geophys., 20, 67–89, https://doi.org/10.1029/rg020i001p00067, 1982.

Wendisch, M., Brückner, M., Burrows, J., Crewell, S., Dethloff, K., Ebell, K., Lüpkes, C., Macke, A., Notholt, J., Quaas, J., Rinke, A., and Tegen, I.: Understanding Causes and Effects of Rapid Warming in the Arctic, Eos, 98, https://doi.org/10.1029/2017eo064803, 2017.

Wendisch, M., Macke, A., Ehrlich, A., Lüpkes, C., Mech, M., Chechin, D., Dethloff, K., Velasco, C. B., Bozem, H., Brückner, M., Clemen, H.-C., Crewell, S., Donth, T., Dupuy, R., Ebell, K., Egerer, U., Engelmann, R., Engler, C., Eppers, O., Gehrmann, M., Gong, X.,

Gottschalk, M., Gourbeyre, C., Griesche, H., Hartmann, J., Hartmann, M., Heinold, B., Herber, A., Herrmann, H., Heygster, G., Hoor, P., Jafariserajehlou, S., Jäkel, E., Järvinen, E., Jourdan, O., Kästner, U., Kecorius, S., Knudsen, E. M., Köllner, F., Kretzschmar, J., Lelli, L., Leroy, D., Maturilli, M., Mei, L., Mertes, S., Mioche, G., Neuber, R., Nicolaus, M., Nomokonova, T., Notholt, J., Palm, M., van Pinxteren, M., Quaas, J., Richter, P., Ruiz-Donoso, E., Schäfer, M., Schmieder, K., Schnaiter, M., Schneider, J., Schwarzenböck, A., Seifert, P., Shupe, M. D., Siebert, H., Spreen, G., Stapf, J., Stratmann, F., Vogl, T., Welti, A., Wex, H., Wiedensohler, A., Zanatta, M., and Zeppenfeld, S.: The Arctic Cloud Puzzle: Using ACLOUD/PASCAL Multiplatform Observations to Unravel the Role of Clouds and Aerosol Particles in Arctic Amplification, Bull. Am. Meteorol. Soc., 100, 841–871, https://doi.org/10.1175/bams-d-18-0072.1, 2019.

Wendisch, M., Brückner, M., Crewell, S., Ehrlich, A., Notholt, J., Lüpkes, C., Macke, A., Burrows, J. P., Rinke, A., Quaas, J., Maturilli, M., Schemann, V., Shupe, M. D., Akansu, E. F., Barrientos-Velasco, C., Bärfuss, K., Blechschmidt, A.-M., Block, K., Bougoudis, I., Bozem, H., Böckmann, C., Bracher, A., Bresson, H., Bretschneider, L., Buschmann, M., Chechin, D. G., Chylik, J., Dahlke, S., Deneke, H., Dethloff, K., Donth, T., Dorn, W., Dupuy, R., Ebell, K., Egerer, U., Engelmann, R., Eppers, O., Gerdes, R., Gierens, R., Gorodetskaya, I. V., Gottschalk, M., Griesche, H., Gryanik, V. M., Handorf, D., Harm-Altstädter, B., Hartmann, J., Hartmann, M., Heinold, B., Herber, A., Herrmann, H., Heygster, G., Höschel, I., Hofmann, Z., Hölemann, J., Hünerbein, A., Jafariserajehlou, S., Jäkel, E., Jacobi, C., Janout, M., Jansen, F., Jourdan, O., Jurányi, Z., Kalesse-Los, H., Kanzow, T., Käthner, R., Kliesch, L. L., Klingebiel, M., Knudsen, E. M., Kovács, T., Körtke, W., Krampe, D., Kretzschmar, J., Kreyling, D., Kulla, B., Kunkel, D., Lampert, A., Lauer, M., Lelli, L., von Lerber, A., Linke, O., Löhnert, U., Lonardi, M., Losa, S. N., Losch, M., Maahn, M., Mech, M., Mei, L., Mertes, S., Metzner, E., Mewes, D., Michaelis, J., Mioche, G., Moser, M., Nakoudi, K., Neggers, R., Neuber, R., Nomokonova, T., Oelker, J., Papakonstantinou-Presvelou, I., Pätzold, F., Pefanis, V., Pohl, C., van Pinxteren, M., Radovan, A., Rhein, M., Rex, M., Richter, A., Risse, N., Ritter, C., Rostosky, P., Rozanov, V. V., Donoso, E. R., Saavedra-Garfias, P., Salzmann, M., Schacht, J., Schäfer, M., Schneider, J., Schnierstein, N., Seifert, P., Seo, S., Siebert, H., Soppa, M. A., Spreen, G., Stachlewska, I. S., Stapf, J., Stratmann, F., Tegen, I., Viceto, C., Voigt, C., Vountas, M., Walbröl, A., Walter, M., Wehner, B., Wex, H., Willmes, S., Zanatta, M., and Zeppenfeld, S.: Atmospheric and Surface Processes, and Feedback Mechanisms Determining Arctic Amplification: A Review of First Results and Prospects of the (AC)[3] Project, Bull. Am. Meteorol. Soc. (published online ahead of print 2022), https://doi.org/10.1175/bams-d-21-0218.1, 2022a.

Wendisch, M., Stapf, J., Becker, S., Ehrlich, A., Jäkel, E., Klingebiel, M., Lüpkes, C., Schäfer, M., and Shupe, M. D.: Effects of variable, ice-ocean surface properties and air mass transformation on the Arctic radiative energy budget, Atmos. Chem. Phys. Discuss. (preprint), 2022, 1–31, https://doi.org/10.5194/acp-2022-614, 2022b.

Wesche, C., Steinhage, D., and Nixdorf, U.: Polar aircraft Polar5 and Polar6 operated by the Alfred Wegener Institute, Journal of Large-scale Research Facilities JLSRF, 2, https://doi.org/10.17815/jlsrf-2-153, 2016.

Zelinka, M. D., Klein, S. A., and Hartmann, D. L.: Computing and Partitioning Cloud Feedbacks Using Cloud Property Histograms. Part II: Attribution to Changes in Cloud Amount, Altitude, and Optical Depth, J. Clim., 25, 3736–3754, https://doi.org/10.1175/jcli-d-11-00249.1, 2012.